

Accurate Brain Extraction using Active Shape Model and Convolutional Neural Networks

Nguyen Ho Minh Duy^a, Nguyen Manh Duy^a, Mai Thanh Nhat Truong^b, Pham The Bao^a, Nguyen Thanh Binh^{a,*}

^a*Department of Mathematics and Computer Science, Ho Chi Minh City University of Science, Ho Chi Minh City, Viet Nam*

^b*Department of Electrical, Electronic and Control Engineering, Hankyong National University, Anseong, Gyeonggi, Republic of Korea*

Abstract

Brain extraction or skull stripping is a fundamental procedure in most of neuroimaging processing systems. The performance of this procedure has had a critical impact on the success of neuroimaging analysis. After several years of research and development, brain extraction still remains a challenging problem. Brain morphology and intensity characteristics are variable and complex, usually because of the variability in conditions of image data acquisition, or abnormalities in data such as tumor regions. These difficulties prevent brain extraction methods from producing acceptable results. In this paper, we propose an effective method for skull stripping in Magnetic Resonance Imaging (MRI) scans named ASM-CNN. Our system is a combination of Active Shape Model (ASM) and Convolutional Neural Network (CNN), taking full advantage of these two methods to achieve remarkable results. Instead of working with 3D structures, we process 2D image sequences in sagittal plane. First, we divide images into different groups such that, in each group, the shapes and structures of brain boundaries have similar appearances. This allows developing precise algorithms for each group in order to produce high performance segmentation results. Second, a modified version of ASM is used to detect the brain boundary in images by utilizing prior knowledge of each group. Finally, CNN and the post-processing methods such as Conditional Random Field, Gaussian Process and some special rules are applied to refine segmentation contour produced by ASM. We compared ASM-CNN with the latest version of five state-of-the-art, publicly available methods, namely BET, BSE, 3DSS, ROBEX and BEAST. The evaluation was carried out by using three public datasets IBSR, LPBA and OASIS. The experimental results show that the proposed method outperforms five states-of-the-art algorithms, surpassing all the other methods by a significant margin in all experiments.

Keywords: skull stripping, brain extraction, convolutional neural network, active shape model, conditional random field, gaussian process

*Corresponding author

Email address: ngtbinh@hcmus.edu.vn (Nguyen Thanh Binh)

1. Introduction

Whole brain segmentation is the problem of extracting brain regions from volumetric data, such as Magnetic Resonance Imaging (MRI) or Computed Tomography (CT) scans. The results of this process is segmentation map indicating brain regions after removing non-brain tissue such as eyes, fat, bone, marrow, and dura. Brain extraction is the first step in most neuroimaging analysis systems which usually consists of brain tissue classification and volumetric measurement [1], template construction [2], and cortical and sub-cortical surface analysis [3]. Early preprocessing steps such as bias field correction can also benefit from brain extraction [4]. Therefore, there is a need for high performance brain extraction methods that can produce accurate segmentation results.

Automatic skull stripping is a solution to replace manual brain delineation for the purpose of reducing processing time and preventing any kind of human bias in the results. This is especially true in large scale studies, where thousands of images with different characteristics and significant anatomical variations are examined. Most skull stripping methods are optimized and validated for MRI T1-weighted images, since high resolution T1-weighted structural images are prevalent in clinical studies [5]. Furthermore, T1-weighted images provide excellent contrast between different brain tissues, making it the leading imaging standard for volumetric measurements [6]. However, segmentation on T1-weighted data is generally a daunting task due to the complex nature of the images (ill-defined boundaries, low contrast) and the lack of standard in image intensity. Several methods have been proposed in the recent years. However, these methods show good performance only on certain datasets, they produce low quality results when the acquisition conditions or study populations change [5].

Existing brain extraction methods can be divided into four categories, namely edge-based, template-based, label fusion with atlas-based and non-local patch based [6]. Edge-based methods focus on detecting edges between brain and non-brain regions by considering differences in appearance of these structures. There are several techniques have been employed such as watershed [7], level set [8], histogram analysis [9], morphological filtering [10], region growing [11], edge detection [12], graph cuts [13], and convolutional neural networks [14]. Although these methods have proven its effectiveness and achieved comparable results, their performance tend to be less accurate when working with pathology, different sites, scanners, and imaging acquisition protocols.

Template-based methods register the subject to a template via affine transform [15] or deformable models [16] to create an initial estimate for the brain mask. After that, the boundary of brain mask is segmented again by a classifier, which helps increase the accuracy of final result. Templates can involve one or more distinctive atlases. Template-based methods are robust, stable in different conditions and highly accurate.

Label fusion with atlas-based techniques, such as Multi-Atlas Propagation and Segmentation (MAPS) [17], Advanced Normalization Tools (ANTs) [18], and Pincram [19], implement registration of multiple atlases to a target subject by using deformable models. After being registered to the target space, the brain masks in all atlases are combined together by using Simultaneous Truth And Performance Level Estimation (STAPLE)

[20] or joint label fusion. Because the main operations of these approaches are registration process, their performance depends on the accuracy of registration and quality of brain mask in each atlas. In addition, the variability representation in brain anatomy usually requires large number of atlases, hence these methods usually are time-consuming and computationally intensive.

The last category is non-local patch based methods. At first, these methods transform atlases to subject space by using affine registration in order to estimate the initial brain mask of the subject. Then, a neighborhood searching process for each small patch, which is around the initial estimates of brain boundary, is performed. Patches are derived from the registered atlases and located within the neighborhood of target patch. Then the patches are associated together and similarity weights are computed to generate the final brain mask. Several methods such as Brain Extraction using non-local Segmentation Technique (BEAST) [21], Multi-cONtrast brain STRipping (MONSTR) [6] are inspired by this ideas and achieved remarkable performance in aspects of both accuracy and robustness. However, one difficulty of this approach is pinpointing optimal setting for parameters such as number of atlases or window size. Additionally, in researches related to disease study, the brain regions in MRI scans usually contain lesion tissues. Therefore, atlases from T1-weighted images may not be optimal for detecting brain boundaries since intensity values of structures such as hemorrhages, tumors, or lesions may be similar to that of non-brain tissues. To overcome this problem, non-local based methods use different MR acquisition protocols to obtain complementary information. As a result, it is a complex task and requires more processing time.

In this research, we present a novel approach for brain extraction in T1-weighted MRI data. Our system is a combination of Active Shape Model (ASM) [22] and Convolutional Neural Network (CNN) [23], hence the name ASM-CNN. Unlike existing methods, our approach consider brain extraction problem as a segmentation task for 2D image sequences in sagittal plane instead of working with 3D structure. This approach has several benefits. First, it allows developing specific algorithms when dealing with images which have different brain boundary silhouettes. Along image sequences, the shape of brain boundaries and brain sizes vary significantly. Especially for sagittal slices located at the beginning and ending parts of 3D MRI volumes, the brain regions are small and the boundaries are very complex. Based on prior knowledge about brain structures, we developed specific rules representing the relationships between brain tissues. These rules was applied directly to control the segmentation process effectively. Second, images in sagittal plane are symmetry across two hemispheres. By utilizing this property, we are able to predict general shape of brain mask based on the positions of slices. This property also enables us to establish more extensive and accurate rules for segmentation.

ASM-CNN comprises three main stages: dividing images into groups, applying ASM to detect the brain boundaries, and finally using CNN also post-processing methods based on Conditional Random Field (CRF), Gaussian Process (GP) and special rules to refine segmentation contour. In the first stage, all images in sagittal plane are divided into three groups, namely group I, II, and III. The number of groups was decided according to our analysis on boundaries of brain masks. The divide of images is performed by a Support

Vector Machine (SVM) classifier and a set of rates learned from data, for the purpose of determining position for each group. In group II and III, images have similar shapes and structures while group I consists of images which have small brain sizes and complex structures. In the next stage, ASM is applied to group II and group III to estimate initial contours for brain mask. After that, these contours are refined using CNN before fed into post-processing based on CRF to obtain the final segmentation. For group I, because the shapes of brain are complex and the sizes of brain regions are smaller than that in other groups, we take the segmentation result of the slice in group II which is right next to the beginning position of group I and use it as an initial brain mask. This brain mask is then fed into CNN for further analysis with specific rules and GP to produce high quality results. The flowchart of our system is given in Figures 1. The main contributions of the proposed method are:

1. Our approach is based on processing 2D images, this helps increase accuracy in segmenting small-sized brain regions while preserving stable performance in overall segmentation.
2. CNN with high-level feature representations is utilized to refine voxels around brain boundaries. In addition, global spatial information of each voxels is combined with features from CNN by using deep neural networks. In this way, the proposed method is able to represent global and local features simultaneously.
3. ASM is applied to different groups. The similarity of brain contours in each group allows ASM to detect the general properties of boundaries, guaranteeing the geometry attributes of object thus enhancing the accuracy of segmentation results.
4. Finally, our framework does not depend on any specific MRI format so that it can be applied effectively in various acquisitions conditions.

The remainder of this paper is organized as follows. In section 2, we introduce several notations, and present the design and algorithms of our system. In section 3, we report the experimental results, where the proposed method was applied to three public datasets, namely IBSR, LPBA, OASIS, and compared with five state-of-the-art brain extraction methods. Section 4 gives further analysis regarding important issues of the proposed method and discussions for future research. The conclusions of this research are presented in Section 5.

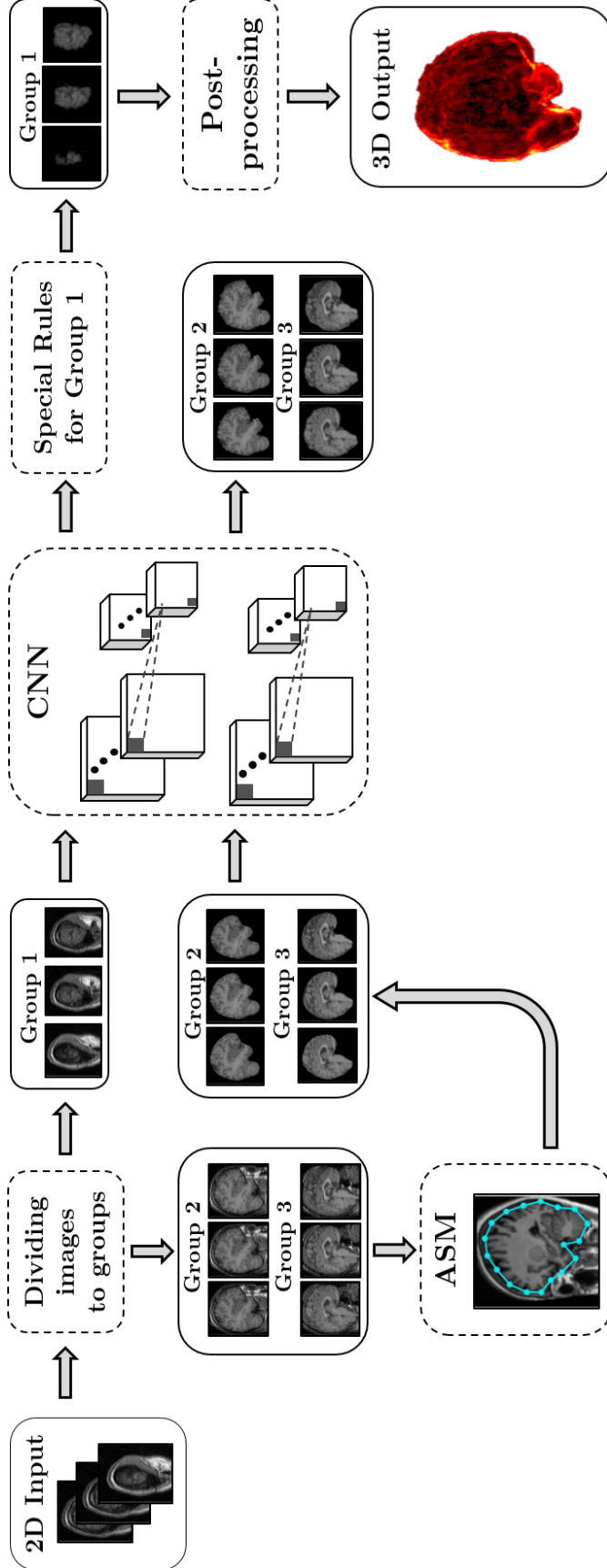


Figure 1: Flowchart of proposed brain extraction algorithm.

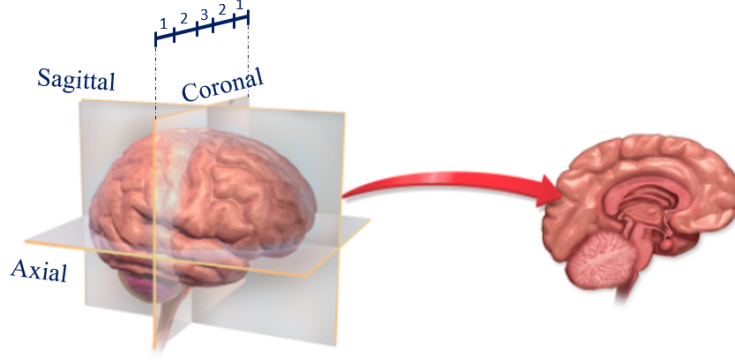


Figure 2: The illustration of the order of three groups in Sagittal plane.

2. Methodology

In neuroimaging, a three-plane coordinate system is used to describe the standard anatomical position of human body. These imaging planes are transverse plane, sagittal plane, and coronal plane. Transverse plane is an X-Z plane and parallel to the ground. Sagittal plane is an Y-Z plane and perpendicular to transverse plane, separating the left side and the right side. Coronal plane is a Y-X plane and perpendicular to sagittal plane, separating the front and the back. In our method, we choose to process 2D sagittal slices because human brains are nearly symmetrical with respect to the mid-sagittal plane. This property enable us predict the general shapes of brain regions more accurately. In the following subsections, we describe three main stages of the proposed method for brain extraction.

2.1. Dividing sagittal slices into groups

The first stage of the algorithm is dividing sagittal slices into groups. The rules for division is based on our analysis on shapes of brain regions. Slices whose brain regions have similar shapes will be put in the same group. Figure 3 indicates some images in group I. The areas of brains in this group are small compared to the sizes of images. Figures 4 and 5 illustrate images in group II and III, respectively. Brain sizes in these groups are relatively large, and in group III, brain regions extend out at the lower left corner of images. Due to the symmetry of brain, from the first to the last sagittal slice, the assigned groups of slices would be from group I to group II, then group III, to group II again and then group I. Figure 2 depicts how three groups are divided in sagittal axis. The main goal of this stage is to group images which have similar brain shapes for the purpose of maximizing the performance of ASM in the next stage.

Before presenting our method in this stage, we introduce the notations used to describe the algorithms:

- $P = \{p_1, p_2, \dots, p_m\}$: the set of people in each dataset, p_i ($1 \leq i \leq m$) is the i th person.
- $N = \{n_1, n_2, \dots, n_m\}$: the set that indicates the numbers of 2D images of a person P where n_j ($1 \leq j \leq m$) is the number of 2D images of p_j .

- $I_{p_j} = \{I_{p_j 1}, I_{p_j 2}, \dots, I_{p_j n_j}\}$: the set of images of person p_j where $I_{p_j k}$ ($1 \leq k \leq n_j$) is the k th image of p_j .
- $G = \{G_1, G_2, G_3\}$: image groups where G_q ($1 \leq q \leq 3$) is the set of images in group q for all people.
- $G_{1p_h} = \{G_{1p_h 1}, G_{1p_h 2}, \dots, G_{1p_h a}\},$
 $G_{2p_h} = \{G_{2p_h 1}, G_{2p_h 2}, \dots, G_{2p_h b}\},$
 $G_{3p_h} = \{G_{3p_h 1}, G_{3p_h 2}, \dots, G_{3p_h c}\},$
represent the set of images in group I, group II, and group III respectively for person p_h where $a+b+c = n_h$.
- M_{12}, M_{23} : the models trained by SVM for classify images between group I and group II, group II and group III.
- R_1, R_2, R_3, R_4 : the rates used for estimating the positions of slices in each group.

In this stage, we train an SVM classifier for the dividing task (Algorithm 1), in which the feature used for training is the histogram of oriented gradients (HOG) [24] extracted from a sub-rectangle. The sub-rectangle in Algorithm 1 is illustrated in Figure 6, which indicates the differences between brain shapes in different groups. Figures 6a and 6b are two adjacent slices from group II and group I, respectively. As shown in this figure, the brain in 6a has a small tail at the lower left part, while the brain in 6b does not. It is apparent that the brain shapes are significantly different even though the slices are adjacent. Similarly, 6c and 6d are two adjacent slices from, respectively, group II and group III. The brain shape in group II is more convex, while that in group III is concave at the lower right part. We utilize these differences to maximize the classification performance of SVM. Algorithm 2 is used to divide sagittal slices of any MRI volumes into groups, using the SVM model produced by Algorithm 1. In the next stage, we use ASM to estimate initial contours for brain masks of slices in group II and group III. For group I, because the shapes of brain are complex and the sizes of brain regions are smaller than that in other groups, we need specific algorithms for this group. The algorithms for brain extraction in group I are detailed in subsection 2.4.

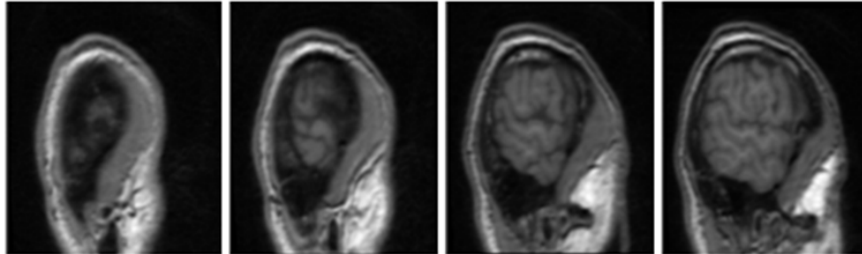


Figure 3: Typical appearances of slices in group I.

Algorithm 1: Training classifiers for dividing images to groups

Input : P

Output: $M_{12}, M_{23}, R_1, R_2, R_3, R_4$

```
1 foreach person  $P_j \in P$  do
2   select  $k_1, k_2, k_3, k_4$  such that:
3    $A = \{I_{p_j 1}, I_{p_j 2}, \dots, I_{p_j k_1}\} \in G_{1p_j}$ 
4    $B = \{I_{p_j k_1+1}, I_{p_j k_1+2}, \dots, I_{p_j k_2}\} \in G_{2p_j}$ 
5    $C = \{I_{p_j k_2+1}, I_{p_j k_2+2}, \dots, I_{p_j k_3}\} \in G_{3p_j}$ 
6    $D = \{I_{p_j k_3+1}, I_{p_j k_3+2}, \dots, I_{p_j k_4}\} \in G_{4p_j}$ 
7   insert:
8    $G_{xp_j}$  to vector  $G_x$  ( $x \in 1, 2, 3$ )
9    $k_y/n_j$  to vector  $Rate_y$  ( $y \in 1, 2, 3, 4$ )
10 end

11 foreach group  $G_i \in G$  do
12   select constant  $k$ 
13   foreach image  $I \in G_i$  do
14      $Rec \leftarrow$  Extract rectangle containing the skull of  $I$  using Algorithm5
15      $SubRec \leftarrow$  Extract sub rectangle from  $Rec$  with  $k$ 
16      $feature \leftarrow$  Calculate feature for  $I$  in  $SubRec$  with  $HOG$ 
17     insert  $feature$  to vector  $F_i$ 
18   end
19 end

20  $M_{12} \leftarrow$  Create model using SVM algorithm,  $F_1, F_2$ 
21  $M_{23} \leftarrow$  Create model using SVM algorithm,  $F_2, F_3$ 
22  $R_{id} \leftarrow mean(Rate_{id})$ ;  $id \in 1, 2, 3, 4$ 
23 return  $M_{12}, M_{23}, R_1, R_2, R_3, R_4$ 
```

Algorithm 2: Dividing images to three groups

Input : $M_{12}, M_{23}, R_1, R_2, R_3, R_4, I_{p_j}$ **Output:** $G_{1p_j}, G_{2p_j}, G_{3p_j}$

```
1  $R_{i_{new}} \leftarrow R_i.n_j$  ( $i \in \{1, 2, 3, 4\}$ ),  $n_j$  is the number images of  $p_j$ 
2 for  $id \leftarrow R_{1,new} - 10$  to  $R_{1,new} + 10$  do
3   if  $M_{12}(I_{p_j id}) == 0$  then
4     insert  $A = \{I_{p_j 1}, I_{p_j 2}, \dots, I_{p_j id-1}\}$  to vector  $G_{1p_j}$ 
5      $R_{1,new} \leftarrow id - 1$ 
6     break
7   end
8 end

9 for  $id \leftarrow R_{2,new} - 10$  to  $R_{2,new} + 10$  do
10  if  $M_{23}(I_{p_j id}) == 0$  then
11    insert  $B = \{I_{p_j R_{1,new}+1}, I_{p_j R_{1,new}+2}, \dots, I_{p_j id-1}\}$  to vector  $G_{2p_j}$ 
12     $R_{2,new} \leftarrow id - 1$ 
13    break
14  end
15 end

16 for  $id \leftarrow R_{3,new} - 10$  to  $R_{3,new} + 10$  do
17  if  $M_{23}(I_{p_j id}) == 1$  then
18    insert  $C = \{I_{p_j R_{2,new}+1}, I_{p_j R_{2,new}+2}, \dots, I_{p_j id-1}\}$  to vector  $G_{3p_j}$ 
19     $R_{3,new} \leftarrow id - 1$ 
20    break
21  end
22 end

23 for  $id \leftarrow R_{4,new} - 10$  to  $R_{4,new} + 10$  do
24  if  $M_{12}(I_{p_j id}) == 1$  then
25    insert  $D = \{I_{p_j R_{3,new}+1}, I_{p_j R_{3,new}+2}, \dots, I_{p_j id-1}\}$  to vector  $G_{2p_j}$ 
26     $R_{4,new} \leftarrow id - 1$ 
27    insert  $E = \{I_{p_j R_{4,new}+1}, I_{p_j R_{4,new}+2}, \dots, I_{p_j n_j}\}$  to vector  $G_{1p_j}$ 
28    break
29  end
30 end
31 return  $G_{1p_j}, G_{2p_j}, G_{3p_j}$ 
```

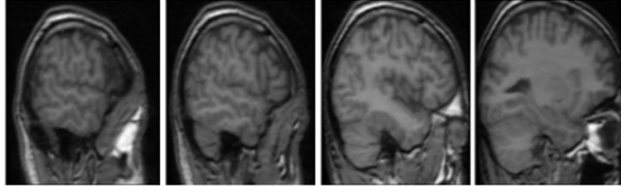


Figure 4: Typical appearances of slices in group II.

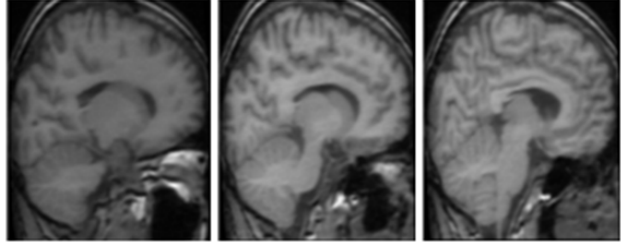


Figure 5: Typical appearances of slices in group III.

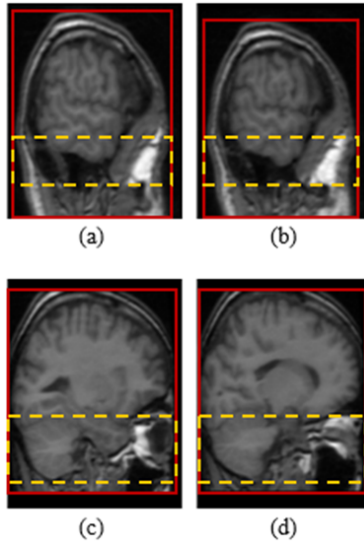


Figure 6: Sub-rectangles and differences between brain shapes in different groups.

2.2. Active shape model with optimal feature

Recently, ASM has been applied successfully in several researches related to medical imaging [25, 26, 27]. In our system, we utilize the similarity of brain shapes of images in the same group by applying ASM with specific model to each group, producing rough segmentations of brain regions which will be refined later. For enhancing the modeling capacity of the gray-level variations around the border of the object, we use a modified version of ASM called Active Shape Model with optimal feature (ASM-OF) [22]. In particular, the optimal displacements for landmarks in original ASM is replaced by using a nonlinear kNN-classifier instead of the linear Mahalanobis distance [28]. We denote some annotations, which are used in section below for describing how ASM-OF is applied to segment each brain image in each group .

- s : the number of training images.
- n : the number of landmark points used to represent each image.
- n_s : the number of new positions evaluated during searching.
- k : the number of points in profile located either inside and outside of the landmark point.
- l_{max} : the number of resolution levels for appearance model.
- n_{grid} : size of $n_{grid} \times n_{grid}$ of points, which are sampled in training process.
- n_{max} : the number of iterations per resolution level.
- k_{NN} : number of neighbors used in k-NN classifier during searching and feature selection.
- f_v : part of variance to be explained by the shape model, determining number of modes.

This stage comprises three subroutines. First, the ASM-OF create a shape model from landmarks in the training set. Second, a k-nearest neighbor classifier (k-NN, [29]) is constructed using a gray-level appearance model. Finally, the shape model and k-NN classifier are combined to produce preliminary estimations of brain masks. The detail of each subroutine is described below.

2.2.1. Shape Model

A brain image in s images is represented by vector x_i by stacking n landmark $((x_1, y_1), \dots, (x_n, y_n))$ as

$$x_i = (x_1, y_1, \dots, x_n, y_n)^T \text{ with } i \in [1, s] \quad (1)$$

Principal component analysis (PCA) is used to calculate the mean shape \bar{x}_s and covariance matrix C , the eigenvectors ϕ_m ($m = 1, \dots, t$) correspond to the first t largest eigenvalues of the covariance matrix, and ϕ_m is the respective variances λ_m as

$$\bar{x}_s = \frac{1}{s} \sum_{i=1}^s x_i, \quad C = \frac{1}{s-1} \sum_{i=1}^s (x_i - \bar{x}_s)(x_i - \bar{x}_s)^T \quad (2)$$

where ϕ_m and λ_m is calculated by singular value decomposition. When brain shape in the training set can be approximated by

$$x_s \approx \bar{x}_s + \Phi_s \mathbf{b}_s \quad (3)$$

where $\Phi_s = (\phi_1 \dots \phi_t)$ is the first t eigenvectors, and b_s is a set of shape parameters which is calculated as

$$\mathbf{b}_s = \Phi_s^T (x_i - \bar{x}_s) \quad (4)$$

In experiment, \mathbf{b}_s is usually bounded by

$$-q\sqrt{\lambda_i} \leq \mathbf{b}_s \leq q\sqrt{\lambda_i} \quad (i = 1, \dots, t) \quad (5)$$

where q varies in the interval $[2, 3]$. The value t eigenvalues to retain is chosen so as to explain a certain proportion f_v of the variance in the training shapes, usually ranging from 90% to 99.5%. The desired number of modes is given by the smallest t such that

$$\sum_{i=1}^t \lambda_i \geq f_v \sum_{i=1}^{2n} \lambda_i \quad (6)$$

2.2.2. Gray-level appearance model with optimal features

The gray-level appearance model that describes the typical image structure around each landmark is obtained by applying k-NN instead from pixel profiles, sampled by using linear interpolation around each landmark, perpendicular to the contour. From each training image and for each landmark a square grid of $n_{grid} \times n_{grid}$ points is defined where n_{grid} is an odd integer and the landmark point at the center of the grid. In our experiments, n_{grid} is set to 5 hence a feature vector has 60 elements which are calculated at 25 points. The output of feature vector is 1 if point is inside the objects or 0 if outside. The k-NN classifier with weight to each vote is $\exp(-d^2)$, where d is the Euclidean distance to each neighbor in the feature space. For selecting the best feature, MannWhitney algorithm is used [30].

Given an input image, each position along the profile is calculated yielding 60 feature images and processing again to create the optimal feature. These features are then fed into k-NN classifier to determine the probability of being inside the object for this pixel. Then we determine the point g_i in the set of point of the profile g such that the object function $f(g)$ is minimized

$$f(g) = \sum_{i=-k}^{-1} g_i + \sum_{i=0}^{+k} (1 - g_i) \quad (7)$$

where g_i is oriented from the outside to the inside of the object, runs from $-k$, to $+k$.

2.2.3. Evolution of the models

After both shape model and k-NN classifiers are constructed from training images, ASM-OF can be applied to segment object by performing the procedures listed below.

- Step 1. Initialize the shape model with \bar{x}_s using (2).

- Step 2. For each landmark, put it at $2n_s + 1$ new locations, evaluate the equation (7) with the k-NN classifier to find and move it to a new position denoted is x_{New} .
- Step 3. Fit the shape model by calculating \mathbf{b}_{sNew} using (4) as (8), and limiting the values of \mathbf{b}_{sNew} using (5).

$$b_{sNew} = \Phi_s^T(x_{New} - \bar{x}_s) \quad (8)$$

where $x_{New} = (x_{1New}, x_{2New}, \dots, x_{nNew})$

- Step 4. Update the shape landmarks using (3) as

$$x_{sNew} \approx \bar{x}_s + \Phi_s \mathbf{b}_{sNew}$$

- Step 5. Iterate steps 2 and 4 up to predefined n_{max} times

Because ASM-OF is only able to capture the general shapes of brain region so the derived boundaries are very smooth. Therefore, in the next stage, we apply convolutional neural networks to refine the preliminary estimations from ASM-OF for the purpose of localizing accurate brain boundaries.

2.3. Convolutional neural networks

Convolutional neural networks (CNNs) are developed from multi-layer perceptrons, which allow exploiting spatial information by using localized convolutional kernels. The main advantage of CNNs is the ability to learn complex, nonlinear and high-dimensional mappings from large data. This attribute makes CNNs achieve remarkable successes in 2D medical image analysis [31, 32]. The typical structure of CNN consists of several pairs of convolutional, sub-sampling layers and multi-layer perceptron. The convolutional layers take input as receptive fields in the previous layer and calculate features while spatial information is preserved. Denote h_j^l is the j -th feature map of the l -th layer and $h_n^{l-1} (n = 1, \dots, N)$ is the m -th feature map of the $(l-1)$ -th layer, the feature map h_j^l is computed by equation:

$$h_j^l = \sigma\left(\sum_{n=1}^N W_{jn}^l * h_n^{l-1} + b^l\right) \quad (9)$$

where W_{jn}^l is the convolutional kernel associated with n -th feature map of the previous layer; b^l is the bias at the l th layer; and σ is the non-linear activation function.

The main operation of sub-sampling is pooling over local neighborhood to reduce the resolution of feature maps. Max-pooling layers are special cases of sub-sampling in which non-max suppression and down-sample the resolution of the feature maps are performed. The multi-layer perceptron with fully connected layers is usually followed several convolutional layers and sub-sampling layers. The final layer of the multi-layer perceptron are values, which are the posterior probability for each class with softmax function.

In our approach, a CNN is used as a classifier to refine the brain contour produced by ASM-OF. Unlike the recent approach using CNNs, our method focuses on pixels located around boundaries of the preliminary

brain masks produced by ASM-OF in the previous stage, instead of processing for all pixels in image. In addition, we also exploit the global spatial information [33] and combine it with feature maps learned from a CNN as a input for multi-layer perceptrons. The details of construction for our CNN are described below.

2.3.1. Input and output space

Denotes that N is the number of slices of an MRI volume, $I_1 = \{I_{11}, \dots, I_{1p}\}$, $I_2 = \{I_{21}, \dots, I_{2q}\}$, $I_3 = \{I_{31}, \dots, I_{3r}\}$ are the sets of images in group I, II, III, respectively where $p+q+r = N$, $M_2 = \{M_{21}, \dots, M_{2q}\}$, $M_3 = \{M_{31}, \dots, M_{3r}\}$ are the sets of brain masks produced by ASM for group II and III. For each image in group II and III, position of pixels around the boundary of $M_i (i \in \{2, 3\})$ with distance 5 pixels are detected by using algorithm 4 (Figure 7). These position then are extracted information based on $I_j (j \in \{2, 3\})$. With images in I_1 , all pixels within the rectangle, which contains the skull, are used as features. The aim of employing a CNN is to classify pixels into brain and non-brain classes.

We extract two types of features for describing each pixel. The first type is local features, which are three adjacent image slices with size 11×11 centered around each pixel. The second type of features is global features, which are combining position (x, y) of each pixel and index z of image where pixel belongs in $(1 \leq z \leq N)$. Figure 8 illustrate the feature extraction step and combine two features in network structure.

In the training process, the total of number brain and non-brain samples are approximately 4000000, 9000000 and 18000000 for IBSR, LPBA and OASIS dataset, respectively. The different in number samples between dataset is mainly caused by the number of subjects in each dataset.

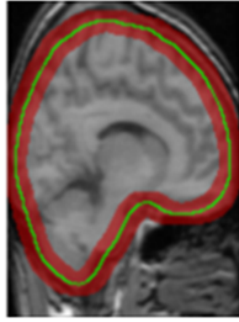


Figure 7: Preliminary brain boundary produced by ASM (green) and surrounding pixels that will be classified by CNN (red).

2.3.2. CNN architecture

Figure 8 illustrates our network structure. It includes three convolutional layers followed by four fully connected layers, including the final two node layer for output. The size of convolutional layers is 3×3 and max pooling uses 2×2 kernel. We configures the depths of the first, second and third convolutional layers to 13, 26 and 39, respectively. The ReLU activation function is applied to the outputs of the convolutional layer.

$$f(x) = \max(0, x) \quad (10)$$

Three vectors from three slices of images obtained from convolutional layers are concatenated with the normalize coordinates to form a new vector. Then this vector is fed into the fully connected layers. The depths of four fully connected layers are 574, 300, 50, and 2, respectively. The final layer has the size of two, indicating the probability of the input pixel belonging to the brain or non-brain class.

2.3.3. Training and Optimization

The aim of CNN is to minimize the cost function:

$$L(w) = \frac{1}{n} \sum_{i=1}^n l(z, f(x, w)) + \frac{\eta}{2} \|w\|^2, \quad (11)$$

for a labeled training set (x_i, z_i) , $i \in (1, n)$ and weights including convolutional kernel weights and bias weight (w_1, \dots, w_L) with a loss function l . The loss function l is defined as:

$$l(z, f(x, w)) = -\frac{1}{N} \sum_{n=1}^N \sum_{m=1}^M B_{m,n} \log(p_{m,n}) \quad (12)$$

where N is the number of training images in the batch, M is the number of classes, $p_{m,n}$ is the probability of the n the example being classified into the m -th class. If the n -th example is classified into the m -th class, $B_{m,n}$ equals 1, otherwise $B_{m,n}$ equals 0.

In equation (11), L_2 regularization is used to penalize the size of w with $\eta = 0.005$ is the coefficient of regularization. The weights w_{t+1} at step $t + 1$ are updated by applied Adam algorithm [34]:

$$m_{t+1} = \beta_1 m_t + (1 - \beta_1) \nabla L(w_t) \quad (13)$$

$$v_{t+1} = \beta_2 v_t + (1 - \beta_2) \nabla L(w_t)^2 \quad (14)$$

$$\hat{m}_{t+1} = \frac{m_{t+1}}{1 - \beta_1^{t+1}} \quad (15)$$

$$\hat{v}_{t+1} = \frac{v_{t+1}}{1 - \beta_2^{t+1}} \quad (16)$$

$$w_{t+1} = w_t - \frac{\alpha \hat{m}_{t+1}}{\sqrt{\hat{v}_{t+1}} + \epsilon} \quad (17)$$

where t is the iteration index, $\alpha = 1e - 04$, $\beta_1 = 0.9$, $\beta_2 = 0.999$ and $\epsilon = 1e - 08$, $m_0 = 0$, $v_0 = 0$.

The weights in each layer at convolutional layer and are initialized from a normal distribution of $N(0, 0.1)$ while weights in multi-layer perceptron layer are created from normal distribution of $N(0, \beta)$ with

$$\beta = \frac{1}{n_{hidden}} \quad (18)$$

where n_{hidden} is the number of hidden layers of previous layer.

The CNN is trained by using mini-batch stochastic gradient descent with batch size of 128. For preventing over-fitting, we use dropout layer after each layer in fully connected layer with rate 0.5.

2.4. Special Rules for Group I

The brain regions in group I are small and have a lot of noise, there would be cases where CNNs produce two regions as segmentation results but it is difficult to automatically determine which area is the brain region. In this paper, we utilized Gaussian Process [35] to overcome this situation.

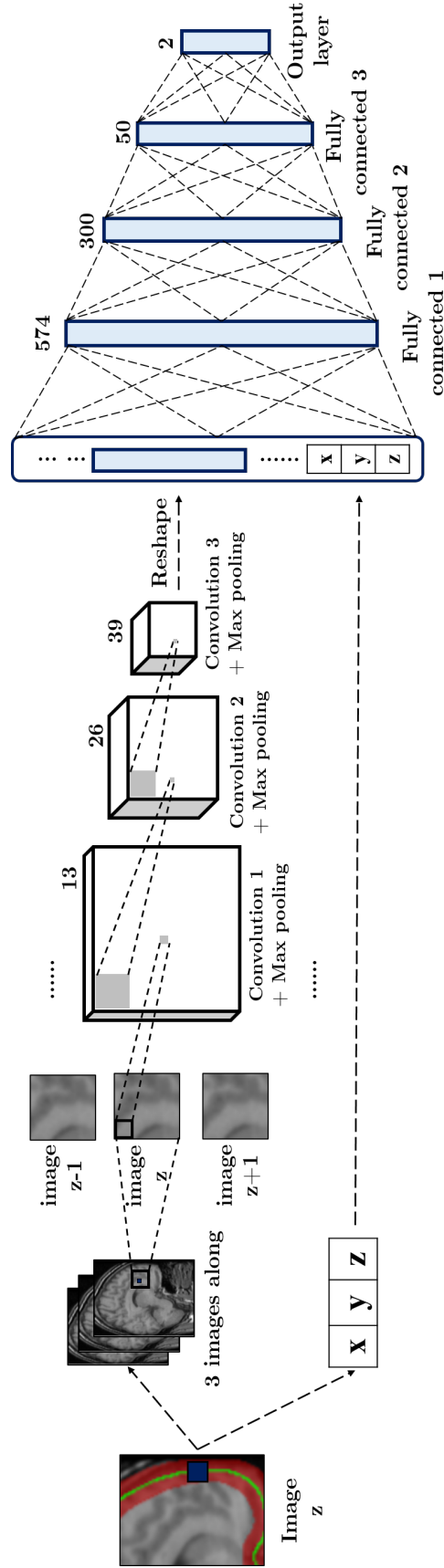


Figure 8: Feature extraction step and our deep neural network structure.

Gaussian Process is used to learn a line that changes center positions of the brain image from the beginning to the end. Based on this line we can predict the center of the cerebral images in region I. Then the closest area closest to the center of gravity is selected for processing. This line is learned based on the Gaussian Process, because it is able to learn complex functions by adjusting the kernel functions.

Figure 9 illustrates the Gaussian Process training results with the IBSR dataset [36]. The blue lines illustrate the change of the cerebral ventricles for each object from start to end position. The training set of IBSR consists of 12 people hence there are 12 blue lines. It is worth noting that the positions of starting and ending slice in MRI volumes are not constants. For example, scans of patient ID 1 start at slice 25 and end at slice 200, scans of patient ID 2 start at slice 20, end at slice 220. Therefore, we normalized the starting and ending slices to $[1, 100]$. The red line illustrates the result of the Gaussian Process.

Figure 10 illustrates the predicted results of the Gaussian Process. The red line illustrates the Gaussian Process's initial prediction for a new subject. After adjusting this prediction, we obtain the blue line which is the final result of the Gaussian Process. The brown line is the ground truth. The adjustment from initial prediction to final result is based on two factors:

- Because of the image acquisition condition, the image of a subject can be shifted, however, the rate of change of the center of the image along the slices remains unchanged. Therefore, it is possible to correctly predict the center of brain regions by translating the initial prediction by a value α .
- The value α is estimated based on a basis that, for each subject, we used a combination of ASM-OF, CNN, and CRF to find the positions of region II and III based on the proposed algorithm. Then we consider the center of all the images in region II and III. By compare the deviation with the result of the Gaussian Process and taking the mean value, we obtain the desired value of α .

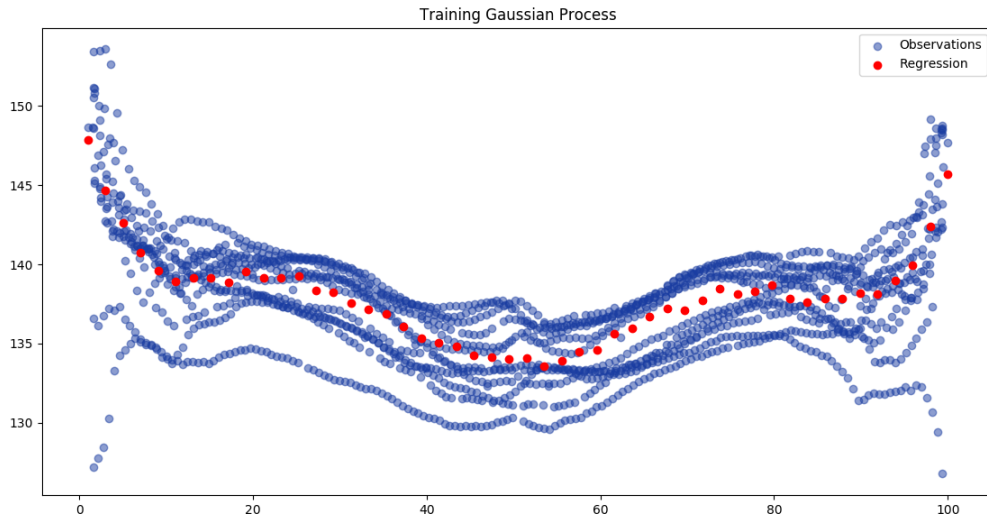


Figure 9: Illustration for training process of Gaussian process in IBSR dataset.

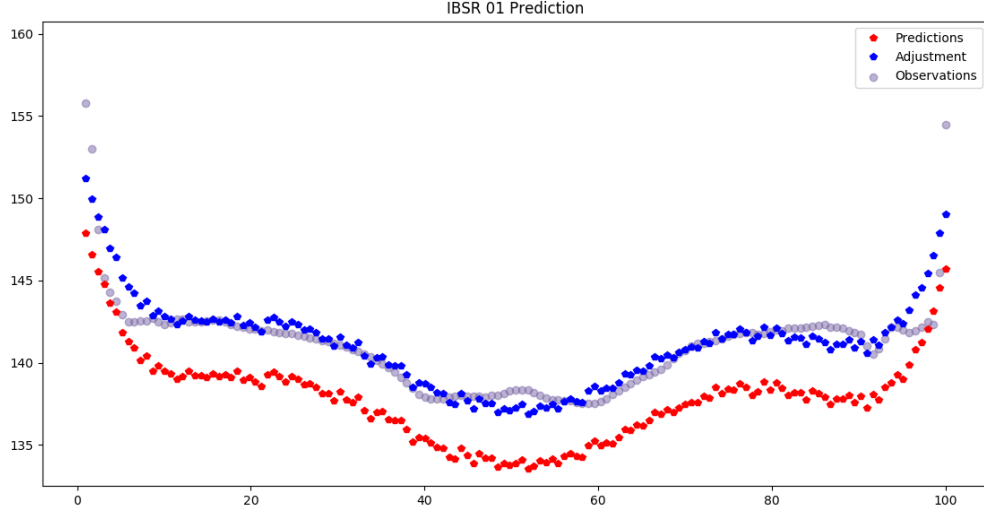


Figure 10: Prediction results of Gaussian process in IBSR dataset.

After the translation and obtaining the blue line, for each slice in region I, we calculate the distance between each connected component in the slice and the predicted value of the Gaussian Process, finally we select the region with the shortest distance. The algorithm 3 describes in detail how images in group I are processed. The list of sub algorithms in the algorithm 3 including *CheckCenter* 6, *CheckArea* 7, *ConvertRange* 5 and *CheckDistance* 8 are presented in Appendices and *CRF* is presented in section 3.

3. Post-processing

Because the main procedures are pixel-wise approaches, the segmentation maps are considerably noisy, decreasing overall accuracy of the brain extraction process significantly. To overcome this problem, we utilize a post-processing technique based on conditional random field (CRF) for validating the extraction results from ASM-OF and CNN, as well as finally refining the segmentation maps. Originally CRF was designed for text segmenting and labeling [37], however there were several success in applying CRF to vision-based applications [38, 39, 40], especially medical imaging [41, 42, 43]. In this research, we use fully connected CRF as the main framework for post-processing because of its capability in producing highly refined segmentation results.

Let \mathbf{I} be an image of size N and \mathbf{x} be a segmentation map of \mathbf{I} , the Gibbs energy of \mathbf{x} is given by

$$E(\mathbf{x}) = \sum_i \varphi_u(x_i) + \sum_{i < j} \varphi_p(x_i, x_j) \quad (19)$$

where x_i, x_j is the label assigned to pixel i, j , respectively. In our system, the properties of segmentation maps are $\mathbf{x} \in \mathcal{L}^N$, $\mathcal{L} \in \{0, 1\}$ which are respective to “brain” (label 1) and “non-brain” (label 0) regions. The unary potential is given by $\varphi_u(x_i) = -\log P(x_i)$, where $P(x_i)$ is the probability of pixel i getting classified as “brain”. This probability is acquired from the output of the main procedure.

Algorithm 3: Process Images in Group I

Input : $C_b \rightarrow C_m, C_{q+1} \rightarrow C_e$: CNN Result Images of Group 0I

F_{m+1}, F_q : 2 Final Segmentation Images in Group II

GPM : Gaussian Process Model

Output: Final Images in Group 0I $F_b \rightarrow F_m, F_{q+1} \rightarrow F_e$

```
1  $Image_1 = F_{m+1}$ 
2  $Image_2 = F_q$ 
3  $\alpha = 0.4$ 
4  $\beta = 1.75$ 
5 for  $i \in [m, m - 1, ..., b + 1, b]$  do
6    $C_i \leftarrow$  Denoise in  $C_i$ 
7    $C_i = CheckCenter(C_i, Image_1)$ 
8    $C_i = CheckArea(C_i, \alpha)$ 
9    $i_{GPM} = ConvertRange(b, e, 1, 100, i)$ 
10   $d_i \leftarrow GPM(i_{GPM})$ 
11   $C_i = CheckDistance(C_i, d_i, \beta)$ 
12   $F_i \leftarrow CRF(C_i)$ 
13   $Image_1 = F_i$ 
14 end
15 for  $j \in [q + 1, q + 2, ..., e - 1, e]$  do
16   $C_j \leftarrow$  Denoise in  $C_j$ 
17   $C_j = CheckCenter(C_j, Image_2)$ 
18   $C_j = CheckArea(C_j, \alpha)$ 
19   $j_{GPM} = ConvertRange(b, e, 1, 100, j)$ 
20   $d_j \leftarrow GPM(j_{GPM})$ 
21   $C_j = CheckDistance(C_j, d_j, \beta)$ 
22   $F_j \leftarrow CRF(C_j)$ 
23   $Image_2 = F_j$ 
24 end
25 return  $F_b \rightarrow F_m, F_{q+1} \rightarrow F_e$ 
```

The pairwise potential $\varphi_p(x_i, x_j)$ is given by

$$\varphi_p(x_i, x_j) = \mu(x_i, x_j) \sum_{m=1}^K w_m k_m(\mathbf{f}_i, \mathbf{f}_j) \quad (20)$$

where $\mu(x_i, x_j)$ follows Potts model, which is

$$\mu(x_i, x_j) = \begin{cases} 1 & x_i \neq x_j \\ 0 & \text{otherwise} \end{cases} \quad (21)$$

The weights are denoted as w_m and $k_m(\mathbf{f}_i, \mathbf{f}_j)$ is the Gaussian kernel depends on feature vectors \mathbf{f}_i and \mathbf{f}_j . Similarly to [39], we employ appearance kernel and smoothness kernel, which are respectively defined as

$$k_1(\mathbf{f}_i, \mathbf{f}_j) = \exp \left(-\frac{|p_i - p_j|^2}{2\sigma_\alpha^2} - \frac{|I_i - I_j|^2}{2\sigma_\beta^2} \right) \quad (22)$$

$$k_2(\mathbf{f}_i, \mathbf{f}_j) = \exp \left(-\frac{|p_i - p_j|^2}{2\sigma_\gamma^2} \right) \quad (23)$$

where p_i, p_j are positions, I_i, I_j are intensity values of pixel i, j . The sigmas ($\sigma_\alpha, \sigma_\beta, \sigma_\gamma$) are used to control the degrees of Gaussian kernels.

The most probable segmentation map \mathbf{x}^* is calculated by

$$\mathbf{x}^* = \arg \min_{\mathbf{x} \in \mathcal{L}^N} E(\mathbf{x}) \quad (24)$$

Because finding the exact minimization is infeasible, the CRF distribution is approximated by a mean-field approximation. The detailed algorithm is presented in [39]. Besides performing mean-field approximation, we need to determine the values of parameters of the model. In our system, we hard-coded the values of w_2 and σ_γ because their effects to segmentation accuracy were insignificant. The other parameters (w_1, σ_α and σ_β) were determined by random search with cross validation.

Figures 11 and 12 illustrate all processing stages of the proposed brain extraction system.

4. Experiments

4.1. Methods for comparison and dataset

In this paper, we consider comparing our proposed system with five well-known methods, namely Brain Extraction Tool (BET) [44], Brain Surface Extractor (BSE) [45], 3DSkullStrip (3DSS) [46], ROBEX [15], and Brain Extraction based on nonlocal Segmentation Technique (BEAST) [21]. The implementations of all algorithms are optimized to work with T1-weighted data. BET is specifically designed for brain extraction tasks. This method utilizes deformable models based on locally adaptive forces to produce brain mask results. In the first stage, the center of the head is estimated. Then, the deformable model with a spherical mesh is applied to fit brain boundaries around this position. BET is very fast and simple but requires manual parameter settings to produce good results. In the experiment, we used BET 2.0, the latest version with several improvements.

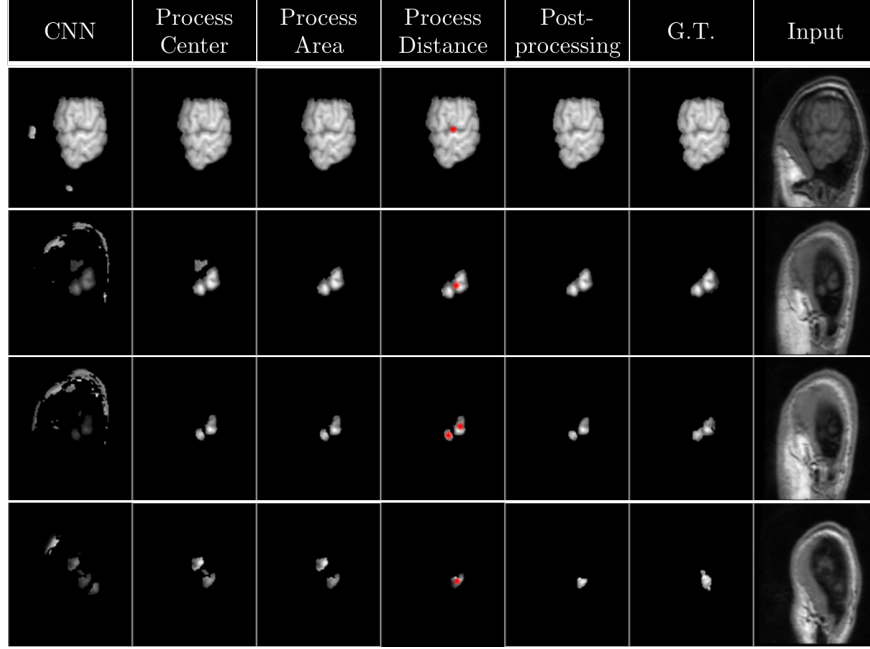


Figure 11: Processing steps for group I.

The next method for comparison is BSE. This method comprises several procedures: anisotropic diffusion filtering, edge detection, and morphological operators. Anisotropic diffusion filtering is used to reduce noise in images while preserving edge boundaries. Marr-Hildreth edge detection is employed to identify the border of the brain regions. Finally, morphological operators such as erosion and dilation is applied to ensure that the result is correct. Although BSE can provide high level of accuracy for whole-brain segmentations, fine parameter tuning is usually required for method to work effectively in specific studies. In this study, we used BSE in BrainSuite15c package, which was released in January 2016.

3DSS is a modification of BET, included in the AFNI package [46]. It uses the spherical surface expansion

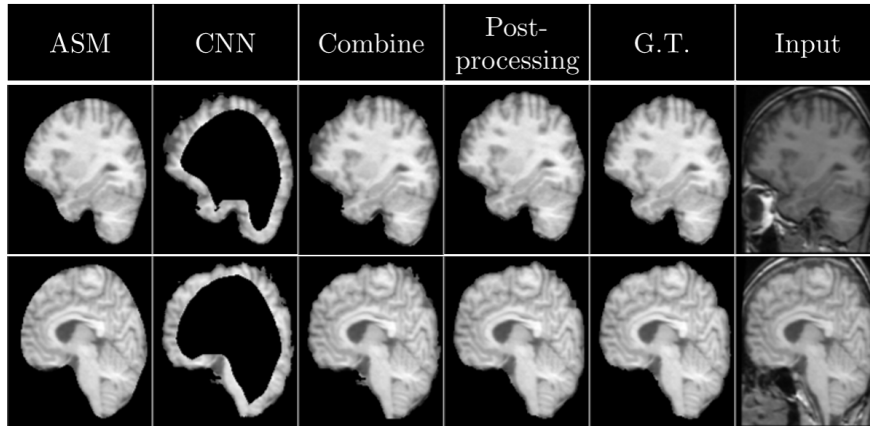


Figure 12: Processing steps for group II and group III.

paradigm, with several modifications to avoid the eyes and ventricles regions, reducing misclassification. Furthermore, not only points inside the surface, but also points located outside are combined together in order to support the evolution of the mesh. In our experiment, we used 3DSS in the AFNI package released on January 2016.

[15] proposed a method called ROBEX. This approach is a combination of a discriminative and a generative model. The random forest classifier is used as a discriminative model to detect voxels located on the brain boundary. The generative model is based on a point distribution model to make sure the shape of the mask is reasonable. In the first stage, ROBEX registers the subject to a template via affine transform. The signal intensities are then normalized and applied bias correction before being fed into the discriminative model. ROBEX is able to work effectively across multiple datasets without requiring any parameter tuning. However, ROBEX uses an adult template as the standard for training the discriminative model, and the target subject is supposed to be aligned. This limits the flexibility of ROBEX in working with different conditions such as imaging modalities and young populations. For evaluating the performance of ROBEX, we used the ROBEX version 1.2 released in November 2013.

The last method used for comparison is BEAST. The ideas of this technique is based on non-local patch matching using multiple atlases. The sum of squared differences metric is used to determine suitable patches. For optimization, input data and prior atlases library need to be normalized in terms of space and intensity. An important characteristics of BEAST is that atlases library needs to be representative of the given data and therefore user is able to add custom priors to the library. When sets of library are selected appropriately, the method can achieve state-of-the-art performance for several data sets even when the data are related to disease such as Alzheimers Disease Neuroimaging Initiative [47].

Three publicly available datasets were used for evaluation. In each dataset, the samples were randomly divided into training and testing groups. The first dataset is Internet Brain Segmentation Repository (IBSR) [36]. This dataset comprises T1-weighted scans ($0.94 \times 1.5 \times 0.94$ mm) of 20 healthy subjects (10 males and 10 females) whose ages vary from 24 to 34. The scans were provided along with manual segmentation performed by experts. Two different scanners were used to acquire the scans. The first scanner, 1.5 Tesla Siemens Magnetom MR System, was used to acquire scans from 4 males and 6 females with a Fast Low Angle SHot (FLASH) pulse sequence and the following parameters: $TR/TE = 40/8$ ms, flip angle 50° , slice thickness 3.1 mm, in-plane resolution 1×1 mm. The scans from the remaining subjects were acquired from a 1.5 Tesla General Electric Signa MR system with a 3D-CAPRY pulse sequence and the following parameters: $TR/TE = 50/9$ ms, flip angle 50° , slice thickness 3.0 mm, in-plane resolution 1×1 mm. Owing to severe striation artifacts existed in some scans, it is challenging to segment on this dataset.

The second dataset is LONI Probabilistic Brain Atlas (LPBA40) [48] which were acquired from healthy volunteers. It contains 40 T1-weighted scans ($0.86 \times 1.5 \times 0.86$ mm) of 20 males and 20 females with the average age is 29.2. The scans were acquired with a 3D spoiled gradient echo sequence on a GE 1.5T system with TR: 10.0-12.5 ms; TE range 4.22-4.5 ms; flip angle 20° . Coronal slices were acquired 1.5 mm apart

with in-plane resolution of 0.86 mm (38 subjects) or 0.78 mm (2 subjects).

The third dataset was obtained from The Open Access Series of Imaging Studies (OASIS) project [49]. It is a cross-sectional and longitudinal collection of 416 subjects aged from 18 to 96. The data were acquired by using T Siemens scanner with a MP-RAGE sequence, $TR/TE/TI/TD = 9.7 \text{ ms}/4.0 \text{ ms}/20 \text{ ms}/200 \text{ ms}$, flip angle 10° . Sagittal slices were acquired 1.5 mm apart with in-plane resolution of 1 mm. We only used 77 T1-weighted scans ($1 \times 1 \times 1 \text{ mm}$) acquired from 55 females and 22 males aged 51.64 ± 24.67 years to make our results comparable to [15]. Differently from IBSR and LPBA40, 20 out of 77 subjects were clinically diagnosed with very mild to moderate Alzheimers disease. Even though the brain masks are not created manually but by a customized method based on registration to an atlas, the results from this method were carefully checked by experts before releasing. This dataset is worthwhile by virtue of including scans from a very diverse subjects with a expansive age range in addition to diseased brains. On account of this, it is sufficient to use this dataset in order to prove the effectiveness and robustness of our approach.

In this research, 6 out of 20 subjects in IBSR dataset were used for training and the 14 remained subjects were for evaluating. Similarly, 12/28 is the number of training/testing subjects in LPBA40 dataset and 22/55 is the ratio for OASIS dataset.

4.2. Setup

The proposed method was implemented in MATLAB and Python. Applying ASM-OF as well as extracting features for CNN were done using MATLAB. The deep neural networks used for training and testing process was implemented in Python because of its various supported deep learning libraries e.g. TensorFlow.

In these experiments, we used the same deep neural network structure for all three datasets, as shown in Figure 8. In the training process, the values of all weights of networks were randomly generated from a normal distribution with mean 0 and standard deviation 0.1. To overcome overfitting problem, we also added dropout layers with the rate 0.5 after each layer in deep neural network. The ReLU function was selected as an activation function in our experiments. The processing time of the training phase varies depending on the size of dataset. It took approximately 3.2 hours for IBSR, 6.4 hours for LPBA40, and 12.8 hours for OASIS to complete the training phase. This process was performed on a workstation with Intel(R) Core(TM) i7-6700K CPU running at 4.00Ghz and an NVIDIA GeForce GTX 980 GPU. The average time for processing one single MRI volume in testing phase is roughly 4 minutes.

4.3. Evaluation Metrics

We evaluated the performance of our brain extraction method by comparing the segmentation results with the ground truth in each dataset. Among several popular metrics used for measuring the distance or similarity between two images, we used the Dice coefficient, the Jaccard index and the Average Hausdorff Distance (AHD). Furthermore, sensitivity and specificity scores were also calculated.

Aforementioned metrics can be derived from the four basic cardinalities of the confusion matrix, which are true positives (TP), false positives (FP), true negatives (TN), and false negatives(FN). TP are voxels

correctly classified as brain tissue while TN consisted of voxels precisely predicted as non-brain tissue. FN are brain tissue voxels in the ground truth but misclassified by the methods. In contrast, FP are incorrectly identified brain tissue voxels.

The Dice coefficient is commonly used to measure repeatability in order to compare directly machine-generated and ground truth segmentation. It is possibly the most-used measure for validating medical segmentations. The Dice coefficient is calculated by

$$D = \frac{2TP}{2TP + FP + FN} \quad (25)$$

The values of this coefficient is in the interval $[0, 1]$ where the maximum value indicates that two segmentation map are identical.

The Jaccard index is another widely used similarity measure and closely related to the Dice coefficient. The relationship of two metrics is represented by

$$D = \frac{2J}{1 + J} \quad (26)$$

hence

$$J = \frac{TP}{TP + FP + FN} \quad (27)$$

Sensitivity and specificity are similar to each other. Sensitivity is essentially how good a prediction is at true positive. Analogously, specificity is a measure of how accurate a prediction is against false positives. However, it is not common to use these two measures for evaluation of medical image segmentation because of their sensibility to segments size. These metrics are defined as follows:

$$Sens = \frac{TP}{TP + FN} \quad (28)$$

$$Spec = \frac{TN}{TN + FP} \quad (29)$$

Differently from other metrics, the AHD is a spatial distance based metrics measuring dissimilarity between two segmentations, where one is the predicted result needs to be evaluated and the other is respective ground truth. These metrics are usually used when the overall accuracy, for instance the contour of the segmentation, of the result is of importance. Because the normal Hausdorff distance is sensitive to outliers, it is recommended to use the AHD which is known to be more stable. The AHD between two segmentation map X and Y is defined by

$$AHD(X, Y) = \max(d(X, Y), d(Y, X)) \quad (30)$$

where $d(X, Y)$ is the directed average distance given by

$$d(X, Y) = \frac{1}{N} \sum_{x \in X} \min_{y \in Y} \|x - y\| \quad (31)$$

5. Results

5.1. Qualitative evaluation

The segmentation results of all method including our proposed in a sagittal plane for IBSR, LPBA and OASIS are illustrated in Figure 13 - 15 respectively. Each figure includes 6 typical testing scans from all three groups (2 scans for each group). Although ASM-CNN approaches the sagittal plane, it also works well and gives correct segmentation in two other planes, which are transverse and coronal plane. Figure 16 shows the comparison between our approach and other methods on each dataset for these two planes.

For the BET, it generally gives good results for almost testing samples. Missing the cerebellum in its segmentation is the crucial problem of this method. Even for scans in group III which are brains in a big size with not so complex structure, BET sometime provides false segmented result (see Figure 13 and Figure 15). This issue appears in IBSR and mostly in OASIS dataset which can be clearly seen in coronal plane in Figure 16. For the LPBA samples it seems to be improved and gets better performance. However, comparing with other methods, it happens more frequent on BET. Moreover, Figure 16 shows that BET often leaves out the lateral ventricles of its segmented result along with BSE and 3DSS. Although fails in group II and III, this method can produce acceptable segmentations on images in group I (see Figure 15).

BSE seems to have the same performance with BET method which also fails at cerebellum segmentation and does not include the ventricles. Different from other methods, sustainability is the main disadvantage of BSE. It can gives excellent results in LPBA dataset but very poor in IBSR and OASIS. This can be seen clearly in II scans in the same group III and same dataset in Figure 13. BSE works well in the first scan although the dura matter and the cranium is oversegmented. However, for the second scan which has higher contrast in the same group III, this method completely fails to produce correctly result. One of the reasons for unstable segmentation is because we employed the default parameters. Hence carefully tuning the parameters is necessary when using BSE. Besides, Figure 13 also shows that this method sometime gives good segmentation for images in group I.

The extracted results obtained by 3DSS, which is a modified version of BET, are slightly better than BET and BSE. 3DSS produces great segmentation in LPBA and its performance decreases in IBSR and OASIS. Unlike BET, segmentation by 3DSS can avoid the eyes (see the second scan in Figure 13) and reduce leakage into the skull although there are some minor oversegmentation at temporal lobe of cerebral hemisphere (see the first scan in Figure 14). The same with BSE, this method leaves the ventricles out in its segmentation. However, the results are extremely sharp at the boundary which sometimes loss the interhemispheric tissue in the segmentation (see Figure 16). Furthermore, the extracted brains in group I by 3DSS are also not good as those from BSE.

Both BEAST and ROBEX all have the higher performance than the aboved methods. They produce precise segmentations of cerebellum which BET and BSE often fails at. Besides, the ventricles, which are usually left out in 3DSS or BSE, are included in the segmentations. However, BEAST gives results sharp as those from 3DSS causing to decrease the accuracy. Moreover, the main problem of ROBEX is that it gives

oversmoothed results, leading to inclusion of dura and gray matter loss [6] (see the second scan in Figure 16). Generally, both can provide accurate extracted brains but ROBEX seems to be slightly better than BEAST. Unfortunately, they both work bad for small size brains in group I, even worse than the aboved methods.

Finally, ASM-CNN provides extremely accurate segmentations in all three datasets. The results obtained by our proposed are the same with those by ROBEX with smoothed boundaries. However we can still keep the gray and dura matter in our extracted brains in most of cases in which they are usually left out by ROBEX (see the second scans in Figure 16). Although there are some minor leakage into the skull in ASM-CNN, it happens least than ROBEX and BEAST with smaller oversegmentation. The critical impact of our method is that it can work precisely for the small size brains in group I where other methods usually fail at. We observe in scans from this group in Figure 13 - 15 that our extractions are identical to the groundtruth even for the tiny size brains (see two last scans in Figure 13). However the final result still has a few false negatives and false positive in some cases because of the complex structure in this group. In spite of some minor incorrect segmentation, ASM-CNN still has a better performance than others with higher accuracy.

5.2. Quantitative evaluation

We use five evaluation metrics which are Dice coefficient, Jaccard index, average Hausdorff distance, sensitivity and specificity to compare our method with others. For the sake of easy comparison, we evaluate all methods in 2D (sagittal plane) and 3D form for each dataset. Table 1 - 3 displays the average and standard deviations (SD) of the metrics for IBSR, LPBA and OASIS dataset on 2D plane respectively. Similarly, Table 4 - 6 shows the accuracy of the results executed on 3D structure. The results of different metrics from evaluated methods on three datasets are depicted by box plots in Figure from 17 to 22 respectively.

Because our approach is working with 2D scans, we formulated the result on 3D structure of other algorithms as 2D images sequences in sagittal plane for the reliable evaluating. Base on the result, all methods prone to getting higher scores on the LPBA dataset in which BSE has significant changes when working on this dataset such as the average of Dice coefficient of this method greatly increases about 9% (85% to 94.27%) for the LPBA scans. BEAST has the highest mean of Specificity with small SD for three datasets although there is no big difference between six methods at this evaluation metric. Surpassing all other algorithms, ASM-CNN gets the best performance with the highest average of Dice overlap (with 0.55 - 1.63% higher than the second), Jaccard index (0.8 - 2.45 % higher) and AHD on three datasets and the best Sensitivity on LPBA and OASIS while ROBEX produces the highest on IBSR. Besides, BSE also achieve the same AHD score on LPBA like ASM-CNN but its SD is higher than us (0.32 compared with 0.19). Furthermore, ASM-CNN not only has outstanding mean of evaluation metric scores but also gets the smallest SD values in Dice coefficient, Jaccard index and Sensitivity which can show the consistency of our method.

Although process with 2D plane, we still create 3D results by combining sequences of scans to make ASM-CNN more comparable with other algorithms. There is a increase at the accuracy of five remain methods

in this type of evaluation with a great improvement at standard deviation. Among the other algorithms, BEAST has major changes in its accuracy for several evaluated metrics on three datasets. For instance, it approximately gains more 3.47 - 5.1% on Dice, Jaccard and Sensitivity metrics. Furthermore, BEAST still provides the highest Specificity which is almost 100% for all dataset. Meanwhile, ROBEX continually obtains the best scores in Sensitivity metric on IBSE and LPBA. Despite not our main approach, the 3D results produced by ASM-CNN are remarkable which can be competitive with others. It preserves the impressive performance which gets the best on 3 dataset at Dice coefficient, Jaccard index, AHD and on OASIS at Sensitivity.

The boxplots in Figure 17 and 20 shows that BSE has a big interquartile range (IQR) on IBSR which means the results given from it are more disperse and have larger variance than other algorithms. However this method has the best performance on LPBA (Figure 18, Figure 21) which gives extremely accurate results and better than others although it has a terrible outlier (about 72% at Dice overlap for 2D evaluation). Indeed, this issue was mentioned above that BSE can provide very accurate segmentations but also may give atrocious results which is based on tuning employed parameters. By contrast, ASM-CNN shows its durable and unaffected by datasets that outperforms than others with high accuracy and small IQR as well as SD on three datasets especially on OASIS (Figure 19, Figure 22). Unfortunately, its Specificity is worse than several methods. However it can be improved by employment a suitable post-processing method to mitigate several false positive in the segmentations.

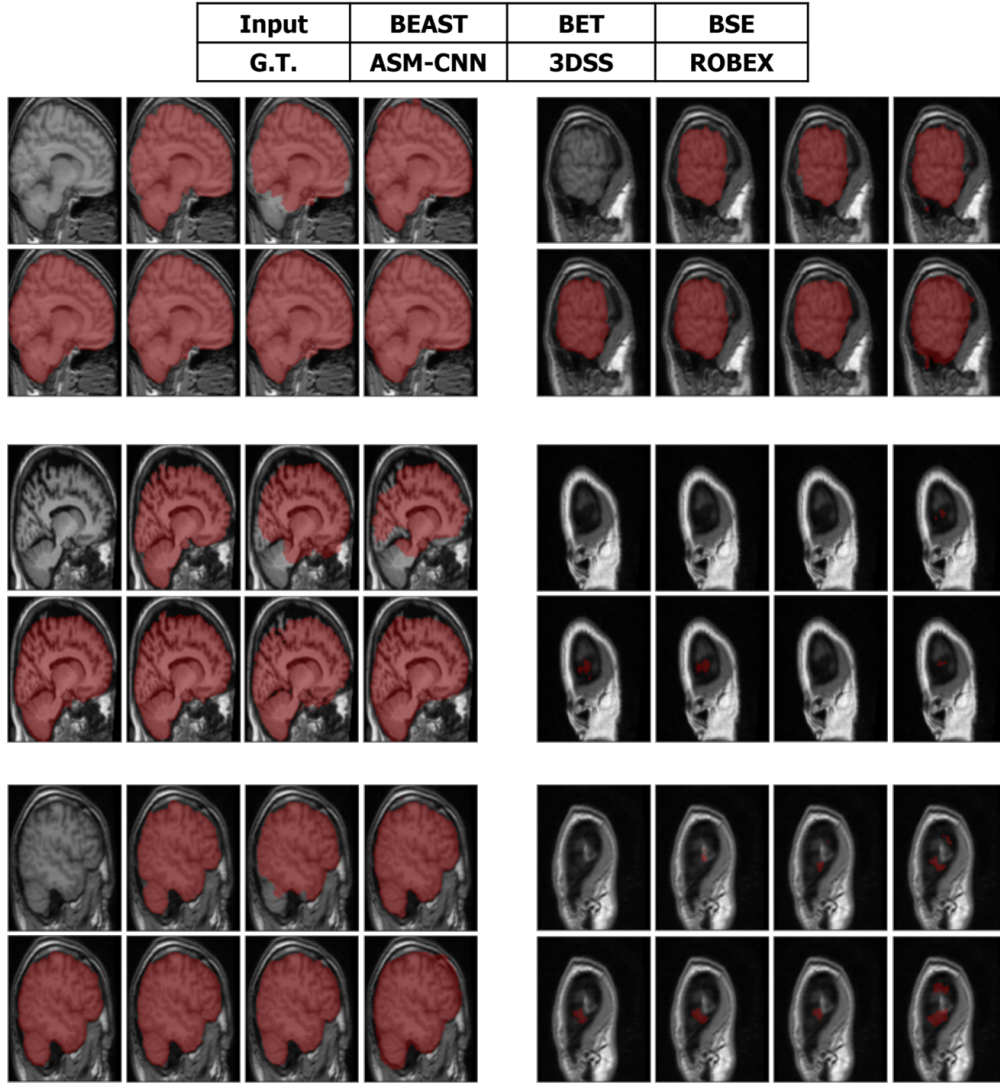


Figure 13: Comparison between ASM-CNN with other methods on IBSR dataset.

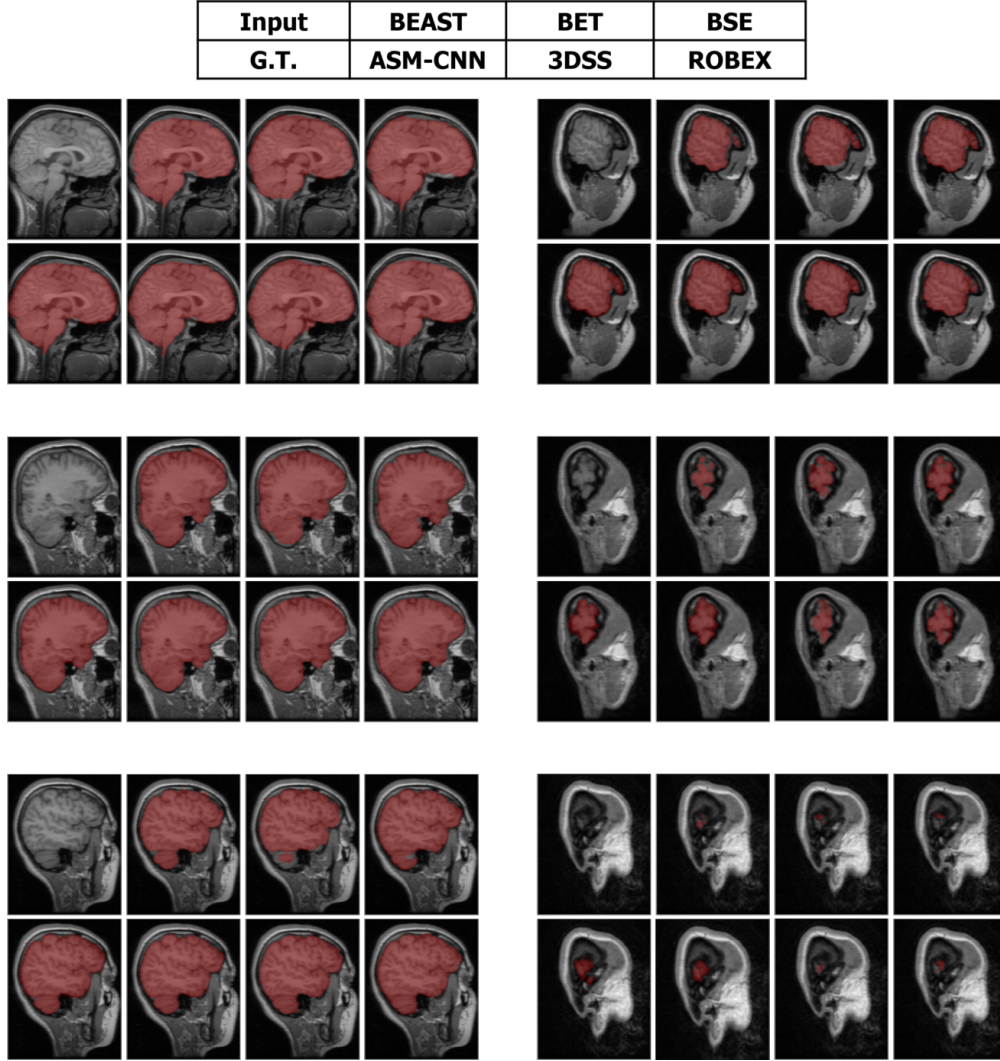


Figure 14: Comparison between ASM-CNN with other methods on LPBA dataset.

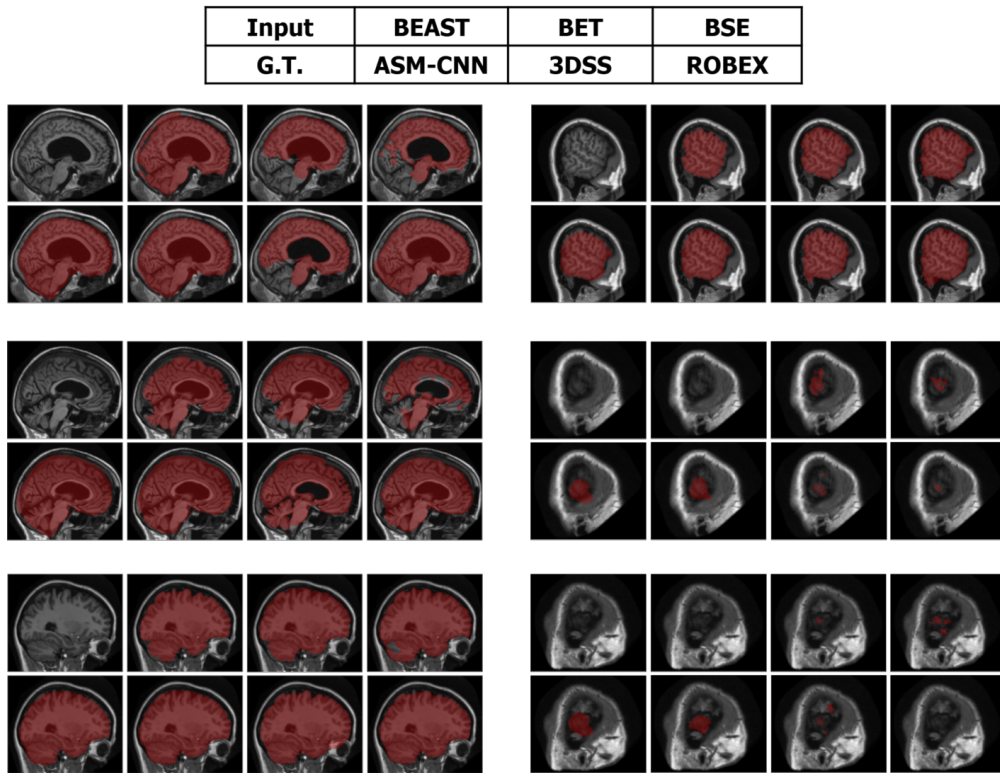


Figure 15: Comparison between ASM-CNN with other methods on OASIS dataset.

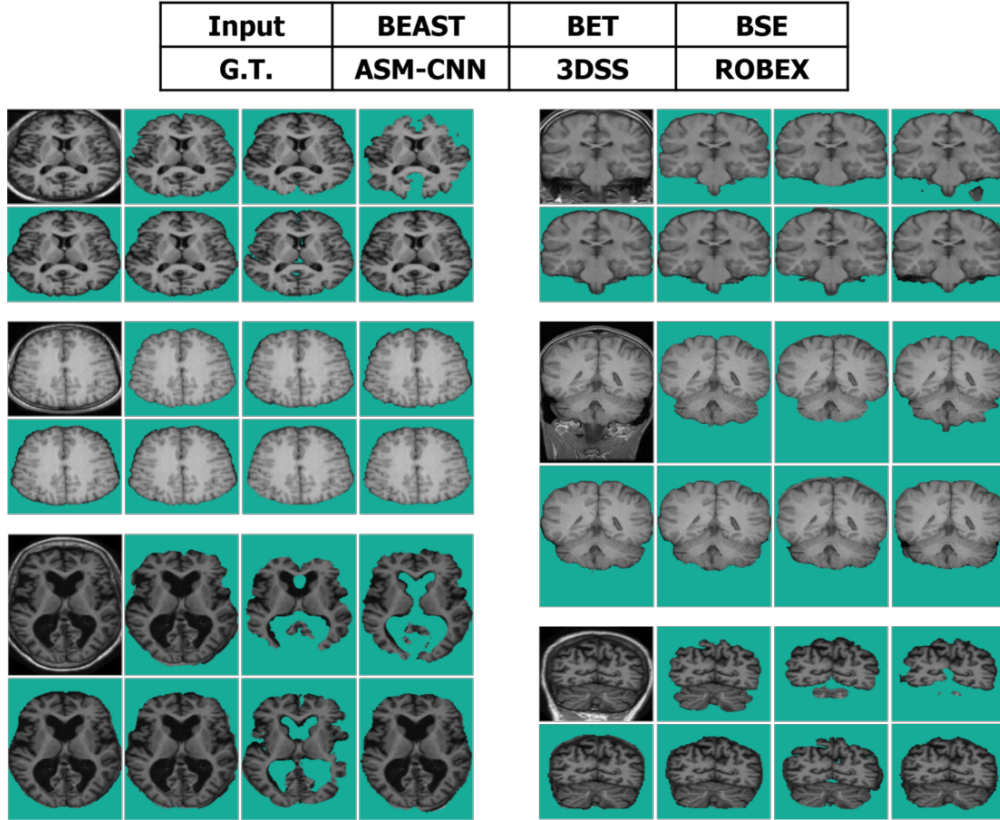


Figure 16: Result image on transverse and coronal plane for IBSR, LPBA, OASIS dataset.

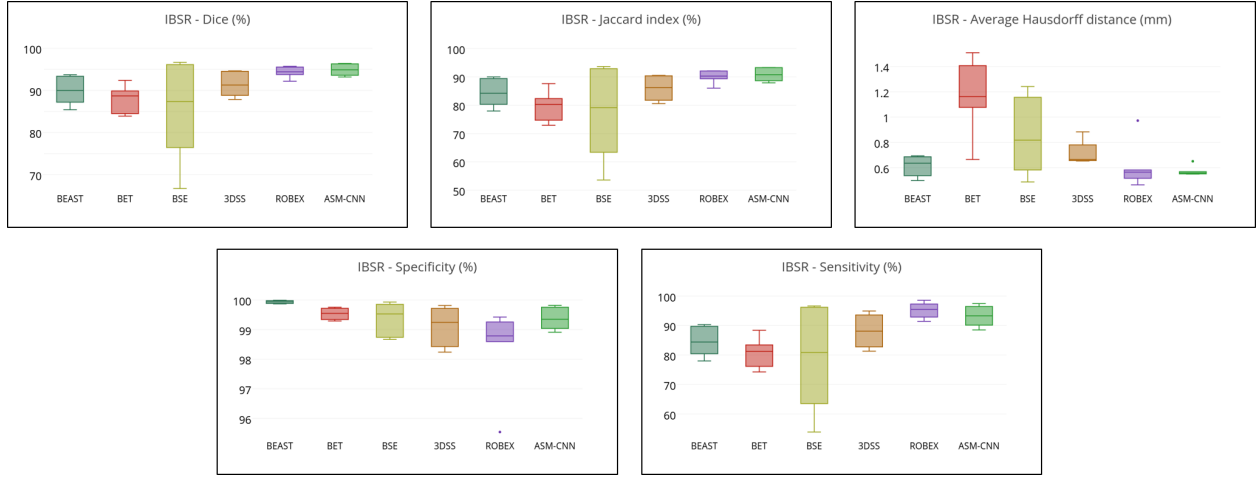


Figure 17: 2D Box plots of Dice coefficient, Jaccard index, Average Hausdorff distance, Sensitivity and Specificity for IBSR dataset.

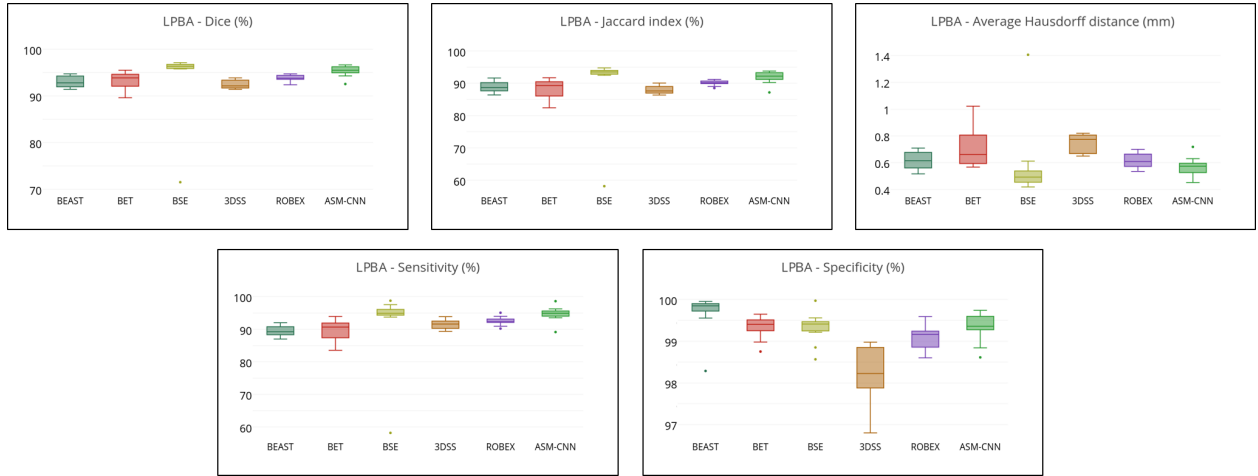


Figure 18: 2D Box plots of Dice coefficient, Jaccard index, Average Hausdorff distance, Sensitivity and Specificity for LPBA dataset.

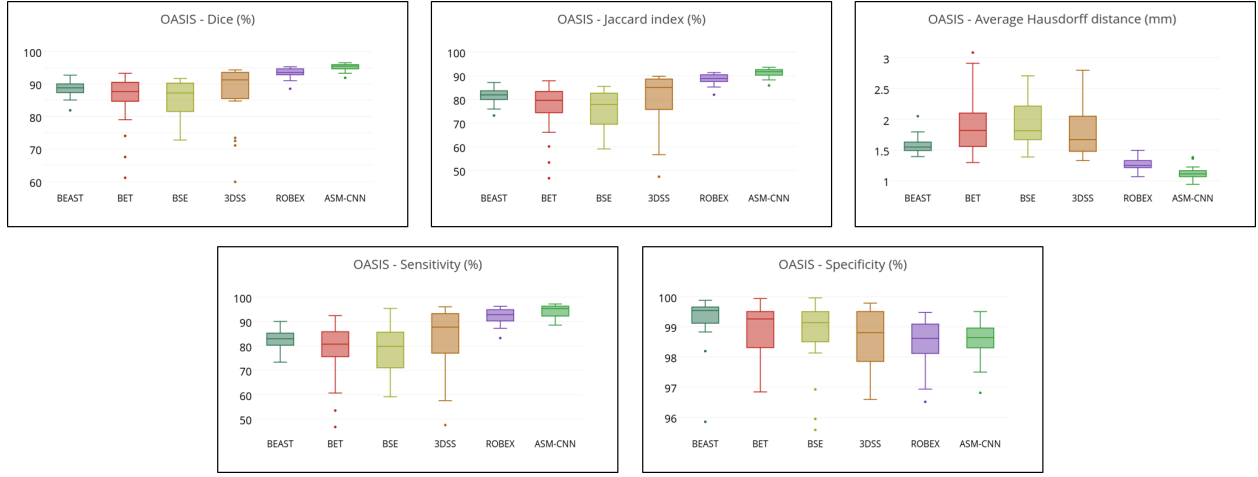


Figure 19: 2D Box plots of Dice coefficient, Jaccard index, Average Hausdorff distance, Sensitivity and Specificity for OASIS dataset.



Figure 20: 3D Box plots of Dice coefficient, Jaccard index, Average Hausdorff distance, Sensitivity and Specificity for IBSR dataset.

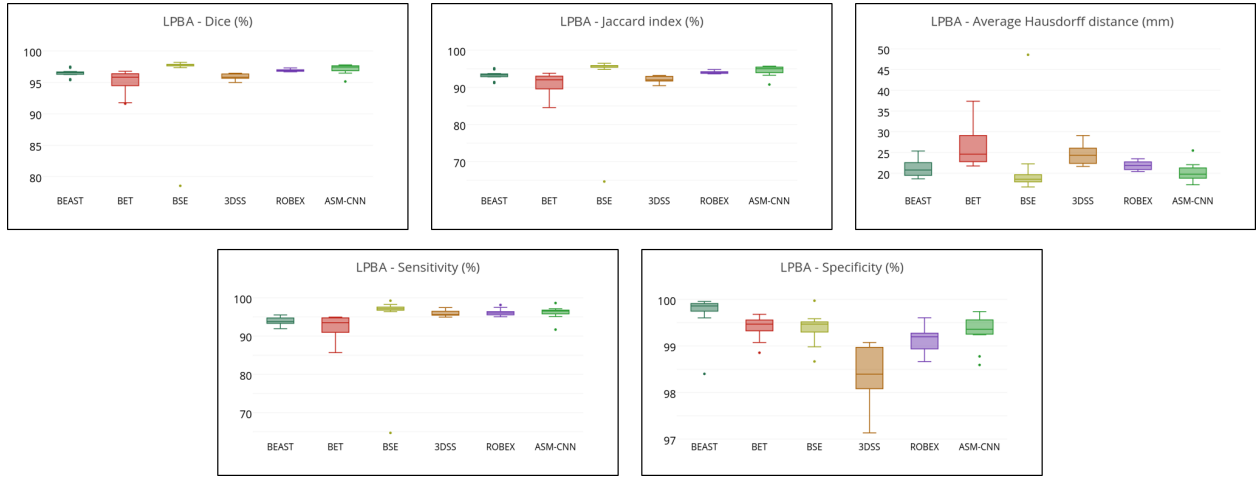


Figure 21: 3D Box plots of Dice coefficient, Jaccard index, Average Hausdorff distance, Sensitivity and Specificity for LPBA dataset.

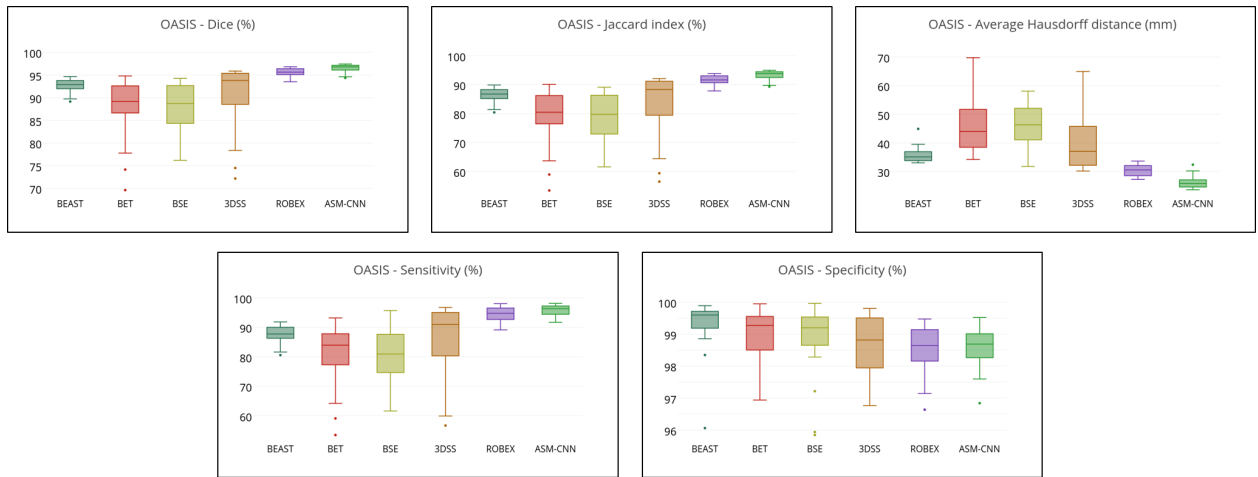


Figure 22: 3D Box plots of Dice coefficient, Jaccard index, Average Hausdorff distance, Sensitivity and Specificity for OASIS dataset.

Method	Dice	Jaccard	Average Hausdorff	Sensitivity	Specificity
BET	87.99 ± 10.49	79.68 ± 12.27	1.16 ± 0.55	80.76 ± 12.25	99.53 ± 0.43
BSE	85.23 ± 16.56	77.17 ± 20.61	0.85 ± 0.41	78.90 ± 21.63	99.36 ± 0.8
3DSS	91.42 ± 13.31	85.99 ± 14.9	0.72 ± 0.22	88.21 ± 15.55	99.1 ± 1.04
ROBEX	94.32 ± 8.13	90.02 ± 10.37	0.61 ± 0.24	95.22 ± 9.43	98.38 ± 1.57
BEAST	90.00 ± 16.51	84.46 ± 17.97	0.61 ± 0.15	84.63 ± 18.02	99.93 ± 0.1
ASM-CNN	94.89 ± 6.33	90.82 ± 9.15	0.57 ± 0.15	93.24 ± 8.53	99.36 ± 0.72

Table 1: 2D Results of different methods in IBSR dataset.

Method	Dice	Jaccard	Average Hausdorff	Sensitivity	Specificity
BET	93.25 ± 8.35	88.17 ± 10.76	0.72 ± 0.28	89.69 ± 10.71	99.34 ± 0.62
BSE	94.37 ± 10.32	90.63 ± 13.51	0.57 ± 0.32	92.41 ± 13.55	99.33 ± 0.66
3DSS	92.47 ± 13.89	87.93 ± 15.27	0.75 ± 0.21	91.46 ± 16.1	98.22 ± 1.6
ROBEX	93.85 ± 12.74	90.12 ± 14.45	0.62 ± 0.17	92.53 ± 14.82	99.08 ± 0.56
BEAST	93.00 ± 13.50	88.83 ± 15.37	0.62 ± 0.16	89.65 ± 15.38	99.67 ± 0.64
ASM-CNN	95.39 ± 7.02	91.87 ± 10.25	0.57 ± 0.19	94.72 ± 7.01	99.33 ± 1.01

Table 2: 2D Results of different methods in LPBA dataset.

Method	Dice	Jaccard	Average Hausdorff	Sensitivity	Specificity
BET	85.34 ± 13.24	76.17 ± 15.41	1.91 ± 0.77	78.17 ± 15.78	98.9 ± 1.05
BSE	85.53 ± 11.68	76.18 ± 14.48	1.94 ± 0.7	78.45 ± 14.96	98.80 ± 1.34
3DSS	87.30 ± 14.49	79.64 ± 17.25	1.81 ± 0.67	82.91 ± 17.8	98.48 ± 1.36
ROBEX	93.44 ± 8.75	88.59 ± 11.16	1.27 ± 0.27	92.1 ± 10.43	98.44 ± 1.05
BEAST	88.56 ± 14.17	81.49 ± 16.27	1.59 ± 0.37	82.71 ± 16.41	99.26 ± 0.99
ASM-CNN	95.07 ± 5.36	91.04 ± 8.46	1.13 ± 0.42	94.36 ± 7.1	98.53 ± 1.46

Table 3: 2D Results of different methods in OASIS dataset.

Method	Dice	Jaccard	Average Hausdorff	Sensitivity	Specificity
BET	89.63 ± 3.86	81.39 ± 6.42	34.99 ± 7.2	82.53 ± 6.09	99.57 ± 0.17
BSE	88.48 ± 9.84	80.50 ± 15.79	32.06 ± 12.88	82.09 ± 17.18	99.42 ± 0.53
3DSS	94.56 ± 2.11	89.75 ± 3.78	24.05 ± 2.2	92.02 ± 5.26	99.18 ± 0.63
ROBEX	96.24 ± 1.28	92.78 ± 2.34	22.72 ± 3.55	97.14 ± 1.63	98.47 ± 1.34
BEAST	94.46 ± 2.27	89.57 ± 4.07	22.27 ± 3.07	89.76 ± 4.2	99.93 ± 0.05
ASM-CNN	96.51 ± 1.03	93.27 ± 1.92	20.63 ± 1.15	95.04 ± 2.92	99.39 ± 0.39

Table 4: 3D Results of different methods in IBSR dataset.

Method	Dice	Jaccard	Average Hausdorff	Sensitivity	Specificity
BET	95.19 ± 1.81	90.87 ± 3.23	26.52 ± 5.1	92.33 ± 3.34	99.40 ± 0.24
BSE	96.19 ± 5.56	93.09 ± 8.96	21.17 ± 8.75	94.66 ± 9.46	99.39 ± 0.32
3DSS	95.85 ± 0.49	92.04 ± 0.91	24.52 ± 2.44	95.90 ± 0.75	98.41 ± 0.60
ROBEX	96.91 ± 0.18	94.00 ± 0.34	21.88 ± 1.07	96.18 ± 0.88	99.13 ± 0.28
BEAST	96.47 ± 0.61	93.20 ± 1.14	21.11 ± 2.08	93.93 ± 1.09	99.72 ± 0.43
ASM-CNN	97.14 ± 0.75	94.46 ± 1.40	20.15 ± 2.19	96.14 ± 1.65	99.33 ± 0.34

Table 5: 3D Results of different methods in LPBA dataset.

Method	Dice	Jaccard	Average Hausdorff	Sensitivity	Specificity
BET	87.99 ± 6.55	79.09 ± 9.72	46.42 ± 10.03	80.73 ± 10.51	98.98 ± 0.82
BSE	88.27 ± 4.88	79.32 ± 7.63	46.16 ± 7.61	81.15 ± 8.84	98.87 ± 1.12
3DSS	90.26 ± 7.15	82.93 ± 10.99	40.54 ± 10.54	85.39 ± 12.37	98.57 ± 1.02
ROBEX	95.64 ± 0.86	91.66 ± 1.57	30.31 ± 1.97	94.36 ± 2.55	98.49 ± 0.79
BEAST	92.72 ± 1.47	86.45 ± 2.52	35.65 ± 2.71	87.59 ± 3.03	99.33 ± 0.82
ASM-CNN	96.50 ± 0.91	93.25 ± 1.68	26.17 ± 2.28	95.82 ± 1.93	98.58 ± 0.65

Table 6: 3D Results of different methods in OASIS dataset.

6. Discussion

In this research, we proposed a system for brain extraction using active shape model and convolutional neural network, hence the name ASM - CNN. The idea behind using ASM is to explore general structures of brain regions, ensuring the consistency of the shape of the object. However, in medical imaging we demand high precision boundaries for segmentation problems, while ASM only provides general shapes and quite smooth. Therefore, we implemented CNN to refine the boundaries produced by ASM. After this step, results from CNN may still be flawed, especially for small and complex brain regions. To overcome this challenge, we proposed some pre-processing techniques based on CRF and Gaussian Process as the final step. CRF with its ability to model the relationships between the pixels being predicted is used to produce a structured output effectively. Gaussian process is applied to learn a non-linear function indicating the changing of the cerebral images from the beginning to the end image due to its power in learning complex functions with a suitable kernel function.

Instead of using whole 3D MRI volume, we decided to approach with 2D scans. This approach allows us to design special rules, adapted for identifying small and complex brain regions, which are often ignored by techniques that focus on processing 3D volume. In addition, we choose 2D scans in sagittal plane to process. Harnessing the symmetry of this plane, we can group brain images into pre-defined groups such that the images in each group have similar shapes. This property enables ASM to learn shape models and appearance model properly in place of learning all shapes, which change significantly when throughout the images.

The proposed method has been compared with five state-of-the-art brain extraction methods. By achieving the highest average of Dice coefficient and Jaccard index with smaller standard deviations, ASM-CNN surpassed all other methods in all experiments. The proposed method also got remarkable scores in other metrics, not only in 2D but also in 3D perspective as well. Despite the inferior result in Specificity, it is still sufficient when it made no significant difference between the top method and ours. ROBEX has shown that it was better than others with many great segmentations. However, the segmentation contours produced by ROBEX were not as sharp as the groundtruth, leading to the increase in false positive. It is also the main weakness of ROBEX when being tested with all three datasets. About BEAST and 3DSS, both methods performed great in general. Their segmentation results were regularly the same as the groundtruth in some cases and their average scores are approximate with each other. Nevertheless, it seemed that BEAST produced the more stable results than 3DSS which had fluctuation in its scores. For instance, there are some cases when 3DSS performed on OASIS dataset, it missed some region of cerebellum, as illustrated in Figure 15. It is worth noting that BEAST was at top in Specificity with the highest average scores in all datasets. For BET and BSE, the quality of their segmentations is worse comparing with others but still acceptable. When dealing with the diversity of brain shapes and contrast in scans, BET and BSE produced some false segmented regions from cerebellum to brain stem which can be easily seen in Figure 13. Their results were also unstable, especially when being tested with OASIS dataset. Moreover, it is shown that BSE

has not been stable on IBSR with the highest standard deviation. On the other hand, BSE was surprisingly good on LBPA, albeit there was still one outlier which had an extremely low accuracy. It can be caused by parameters tuning because BSE is extremely sensitive to these values. For example, when default parameter values were used in LPBA, this tool has obtained superb results. But it was totally different when BSE was applied to other dataset like IBSR or OASIS.

It is worth noting that the properties of datasets affected the performance of brain extraction methods. Due to using two scanner to acquire MR images, IBSR comprises many heterogeneous scans with many obvious artifacts. Besides, this dataset also has the lowest resolution and most anisotropic voxels. LPBA has better resolution images with less noise but it is also fairly anisotropic. OASIS does not have lots of noises and it is isotropic, but it includes some diagnosed Alzheimers disease subjects. Therefore, all methods performed well on LBPA and got the results which did not have any clearly differences. But for other datasets such as IBSR and OASIS, ASM-CNN has shown its remarkable performance when comparing with others, especially in OASIS. It is because the contour refinement by CNN and post-processing by CRF and Gaussian process have done their duty impressively which produced sharp brain boundaries as groundtruth. Furthermore, combining with specific rules for particular groups helped our method overcome the small brain region problems. Our result for this phenomenon is demonstrated in Figure 13. It has to be noted that five other methods were run with the default parameters values. Hence, all the experimental evaluation can be reproduced.

In our system, ASM is used to keep the original structures. However, ASM can only work effectively when the shapes of the objects to be similar to the trained active appearance model. Therefore, the algorithm will likely produce poor results when processing unusual shapes. Unfortunately in medical imaging, the data are usually obscured by noise due to limitations of image acquisition systems, or the shapes and distributions of images are not included in training data. In such cases, ASM may produce severely imprecise boundaries even CNN cannot verify or refine. In the future work, we intend to study the techniques based on deep learning for the purpose of constructing better models for shape and appearance. In addition, with improvements in the future, such as GPU optimization, we believe that the proposed approach can be applied widely in clinical applications because of its fine and robust performance.

7. Conclusion

In this article, we proposed a novel method for brain extraction in magnetic resonance images, namely ASM-CNN. The method was named after its main components: Active Shape Model and Convolutional Neural Network. Unlike existing approaches, ASM-CNN processes 2D sequences of images instead of 3D brain structures. For each 2D scan, first we use a improved version of ASM is Active Shape Model with optimal feature to produce a rough estimate of the brain region, its boundary is then refined by a CNN, which is constructed and trained with several special rules. Finally, the brain region is post-processed by conditional random field and Gaussian process. The proposed approach has shown its consistency in performance, it can

produce high accuracy segmentations in all cases, even when the brain regions are small and scattered. In the experiments, our method achieved remarkable Dice coefficients and Jaccard indexes for the whole three datasets (IBSR, LPBA and OASIS) in 2D scans as well as 3D structures, surpassed the performance of five other state-of-the-art methods (BET, BSE, 3DSS, BEAST and ROBEX).

Acknowledgment

We would like to thank the National Foundation for Science and Technology Development (NAFOSTED), University of Science VNU - HCM, and Business Intelligence LAB at University of Economics and Law, Viet Nam for supporting us throughout this paper.

Appendices

Algorithm 4: *MergeSlice*(X, Y, α)

Input : Two binary images X, Y ; Open distance α

Output: Binary image Z created by combining X and Y

- 1 $O \leftarrow \text{OpenBoundary}(Y, \alpha)$
 - 2 $\text{Core} \leftarrow Y \setminus O$ and $\text{Boundary} \leftarrow X \cap O$
 - 3 $Z \leftarrow \text{Core} \cup \text{Boundary}$
 - 4 Apply morphology to fill small holes in Z (if exists)
 - 5 **return** Z
-

Algorithm 5: *ConvertRange* – Convert a value x_{AB} in range $[A, B]$ to range $[C, D]$

Input : A, B, C, D, x_{AB}

Output: x_{CD}

- 1 $x_{CD} = C + (x_{AB} - A) * (D - C) / (B - A)$
 - 2 **return** x_{CD}
-

Algorithm 6: *CheckCenter* – Remove components in image X whose center is not in image Y to create image Z

Input : X, Y

Output: Z

```
1  $Z = X$ 
2  $bbox \leftarrow$  the smallest bounding box surrounding all components in  $Y$ 
3 foreach component  $c_i$  in  $Z$  do
4    $center_i \leftarrow$  Coordinates of the center of  $c_i$ 
5   if  $center_i$  is not in  $bbox$  then
6     Remove  $c_i$  out of  $Z$ 
7   end
8 end
9 return  $Z$ 
```

Algorithm 7: *CheckArea* – Remove small components in image X with the coefficient α to create image Y

Input : X, α

Output: Y

```
1  $Y = X$ 
2 foreach component  $c_i$  in  $Y$  do
3    $a_i \leftarrow$  Area of  $c_i$ 
4 end
5  $a_{max} \leftarrow \max \{a_i\}$ 
6  $a_{threshold} = \alpha * a_{max}$ 
7 foreach component  $c_i$  in  $Y$  do
8   if  $a_i < a_{threshold}$  then
9     Remove  $c_i$  out of  $Y$ 
10  end
11 end
12 return  $Y$ 
```

Algorithm 8: *CheckDistance* – Remove components having small distance in image X with the coefficient β to create image Y

Input : X, d, β

Output: Y

```

1  $Y = X$ 
2 foreach component  $c_i$  in  $Y$  do
3    $center_i \leftarrow$  Coordinates of the center of  $c_i$ 
4    $dif_i = |d - \|center_i\|_2|$ 
5 end
6  $dif_{min} \leftarrow \min \{dif_i\}$ 
7  $dif_{threshold} = \beta * dif_{min}$ 
8 foreach component  $c_i$  in  $Y$  do
9   if  $dif_i > dif_{threshold}$  then
10    Remove  $c_i$  out of  $Y$ 
11   end
12 end
13 return  $Y$ 

```

References

References

- [1] S. Jiang, W. Zhang, Y. Wang, Z. Chen, Brain extraction from cerebral MRI volume using a hybrid level set based active contour neighborhood model, *BioMedical Engineering OnLine* 12 (1) (2013) 31. doi:10.1186/1475-925X-12-31.
- [2] J. A. Maldjian, J. B. Daunais, D. P. Friedman, C. T. Whitlow, Vervet MRI atlas and label map for fully automated morphometric analyses, *Neuroinformatics* 12 (4) (2014) 543–550. doi:10.1007/s12021-014-9231-8.
- [3] A. M. Dale, B. Fischl, M. I. Sereno, Cortical surface-based analysis: I. segmentation and surface reconstruction, *NeuroImage* 9 (2) (1999) 179–194. doi:10.1006/nimg.1998.0395.
- [4] S. Sharma, V. Noblet, F. Rousseau, F. Heitz, L. Rumbach, J.-P. Armspach, Evaluation of brain atrophy estimation algorithms using simulated ground-truth data, *Medical Image Analysis* 14 (3) (2010) 373–389. doi:10.1016/j.media.2010.02.002.

- [5] P. Kalavathi, V. B. S. Prasath, Methods on skull stripping of MRI head scan images—a review, *Journal of Digital Imaging* 29 (3) (2016) 365–379. doi:10.1007/s10278-015-9847-8.
- [6] S. Roy, J. A. Butman, D. L. Pham, Robust skull stripping using multiple MR image contrasts insensitive to pathology, *NeuroImage* 146 (2017) 132–147. doi:10.1016/j.neuroimage.2016.11.017.
- [7] R. Beare, J. Chen, C. Adamson, T. Silk, D. Thompson, J. Yang, V. Anderson, M. Seal, A. Wood, Brain extraction using the watershed transform from markers, *Frontiers in Neuroinformatics* 7 (2013) 32. doi:10.3389/fninf.2013.00032.
- [8] J. Hwang, Y. Han, H. Park, Skull-stripping method for brain MRI using a 3D level set with a speedup operator, *Journal of Magnetic Resonance Imaging* 34 (2) (2011) 445–456. doi:10.1002/jmri.22661.
- [9] A. G. Balan, A. J. Traina, M. X. Ribeiro, P. M. Marques, C. T. Jr., Smart histogram analysis applied to the skull-stripping problem in t1-weighted MRI, *Computers in Biology and Medicine* 42 (5) (2012) 509–522. doi:10.1016/j.compbiomed.2012.01.004.
- [10] O. Gambino, E. Daidone, M. Sciortino, R. Pirrone, E. Ardizzone, Automatic skull stripping in MRI based on morphological filters and fuzzy c-means segmentation, in: 2011 Annual International Conference of the IEEE Engineering in Medicine and Biology Society, IEEE Computer Society, Washington, DC, USA, 2011, pp. 5040–5043.
- [11] K. Somasundaram, P. Kalavathi, Brain segmentation in magnetic resonance human head scans using multi-seeded region growing, *The Imaging Science Journal* 62 (5) (2014) 273–284. doi:10.1179/1743131X13Y.0000000068.
- [12] T. K. Sreeja, A. Mohammed, J. J. Kumari, A skull-stripping method based on modified morphological processing, in: 2011 International Conference on Signal Processing, Communication, Computing and Networking Technologies, IEEE Computer Society, Washington, DC, USA, 2011, pp. 313–316.
- [13] S. A. Sadananthan, W. Zheng, M. W. Chee, V. Zagorodnov, Skull stripping using graph cuts, *NeuroImage* 49 (1) (2010) 225–239. doi:10.1016/j.neuroimage.2009.08.050.
- [14] J. Kleesiek, G. Urban, A. Hubert, D. Schwarz, K. Maier-Hein, M. Bendszus, A. Biller, Deep MRI brain extraction: A 3D convolutional neural network for skull stripping, *NeuroImage* 129 (Supplement C) (2016) 460–469. doi:10.1016/j.neuroimage.2016.01.024.
- [15] J. E. Iglesias, C. Y. Liu, P. M. Thompson, Z. Tu, Robust brain extraction across datasets and comparison with publicly available methods, *IEEE Transactions on Medical Imaging* 30 (9) (2011) 1617–1634. doi:10.1109/TMI.2011.2138152.
- [16] Y. Wang, J. Nie, P.-T. Yap, F. Shi, L. Guo, D. Shen, Robust deformable-surface-based skull-stripping for large-scale studies, in: Proceedings of the 14th International Conference on Medical Image Computing

and Computer-assisted Intervention - Volume Part III, Springer-Verlag, Berlin, Heidelberg, 2011, pp. 635–642.

- [17] K. K. Leung, J. Barnes, M. Modat, G. R. Ridgway, J. W. Bartlett, N. C. Fox, S. Ourselin, Brain MAPS: an automated, accurate and robust brain extraction technique using a template library, *NeuroImage* 55 (3) (2011) 1091–1108. doi:10.1016/j.neuroimage.2010.12.067.
- [18] B. B. Avants, N. J. Tustison, M. Stauffer, G. Song, B. Wu, J. C. Gee, The insight toolkit image registration framework, *Frontiers in Neuroinformatics* 8 (2014) 44. doi:10.3389/fninf.2014.00044.
- [19] R. A. Heckemann, C. Ledig, K. R. Gray, P. Aljabar, D. Rueckert, J. V. Hajnal, A. Hammers, Brain extraction using label propagation and group agreement: Pincram, *PLOS ONE* 10 (7) (2015) 1–18. doi:10.1371/journal.pone.0129211.
- [20] S. K. Warfield, K. H. Zou, W. M. Wells, Simultaneous truth and performance level estimation (STAPLE): an algorithm for the validation of image segmentation, *IEEE Transactions on Medical Imaging* 23 (7) (2004) 903–921. doi:10.1109/TMI.2004.828354.
- [21] S. F. Eskildsen, P. Coupé, V. Fonov, J. V. Manj, K. K. Leung, N. Guizard, S. N. Wassef, L. R. Østergaard, D. L. Collins, BEaST: brain extraction based on nonlocal segmentation technique, *NeuroImage* 59 (3) (2012) 2362–2373. doi:10.1016/j.neuroimage.2011.09.012.
- [22] T. Cootes, C. Taylor, D. Cooper, J. Graham, Active shape models-their training and application, *Computer Vision and Image Understanding* 61 (1) (1995) 38–59. doi:10.1006/cviu.1995.1004.
- [23] Y. Lecun, L. Bottou, Y. Bengio, P. Haffner, Gradient-based learning applied to document recognition, *Proceedings of the IEEE* 86 (11) (1998) 2278–2324. doi:10.1109/5.726791.
- [24] N. Dalal, B. Triggs, Histograms of oriented gradients for human detection, in: 2005 IEEE Computer Society Conference on Computer Vision and Pattern Recognition (CVPR’05), IEEE Computer Society, Washington, DC, USA, 2005, pp. 886–893 vol. 1.
- [25] M. Esfandiarkhani, A. H. Foruzan, A generalized active shape model for segmentation of liver in low-contrast CT volumes, *Computers in Biology and Medicine* 82 (2017) 59–70. doi:10.1016/j.combiomed.2017.01.009.
- [26] H. El-Rewaidy, E. S. Ibrahim, A. S. Fahmy, Segmentation of the right ventricle in MRI images using a dual active shape model, *IET Image Processing* 10 (10) (2016) 717–723. doi:10.1049/iet-ipr.2016.0073.
- [27] C. Santiago, J. C. Nascimento, J. S. Marques, A new robust active shape model formulation for cardiac MRI segmentation, in: 2016 IEEE International Conference on Image Processing (ICIP), IEEE Computer Society, Washington, DC, USA, 2016, pp. 4112–4115.

- [28] B. Van Ginneken, A. F. Frangi, J. J. Staal, B. M. ter Haar Romeny, M. A. Viergever, Active shape model segmentation with optimal features, *IEEE transactions on medical imaging* 21 (8) (2002) 924–933. doi:10.1109/TMI.2002.803121.
- [29] N. S. Altman, An introduction to kernel and nearest-neighbor nonparametric regression, *The American Statistician* 46 (3) (1992) 175–185. doi:10.1080/00031305.1992.10475879.
- [30] H. B. Mann, D. R. Whitney, On a test of whether one of two random variables is stochastically larger than the other, *The Annals of Mathematical Statistics* 18 (1) (1947) 50–60. doi:10.1214/aoms/1177730491.
- [31] L. K. Tan, Y. M. Liew, E. Lim, R. A. McLaughlin, Convolutional neural network regression for short-axis left ventricle segmentation in cardiac cine mr sequences, *Medical Image Analysis* 39 (Supplement C) (2017) 78–86. doi:10.1016/j.media.2017.04.002.
- [32] M. Havaei, A. Davy, D. Warde-Farley, A. Biard, A. Courville, Y. Bengio, C. Pal, P.-M. Jodoin, H. Larochelle, Brain tumor segmentation with deep neural networks, *Medical Image Analysis* 35 (Supplement C) (2017) 18–31. doi:10.1016/j.media.2016.05.004.
- [33] X. Liu, F. Chen, Automatic segmentation of 3-d brain mr images by using global tissue spatial structure information, *IEEE Transactions on Applied Superconductivity* 24 (5) (2014) 1–5. doi:10.1109/TASC.2014.2347316.
- [34] D. P. Kingma, J. Ba, Adam: A method for stochastic optimization, arXiv preprint arXiv:1412.6980.
- [35] C. Rasmussen, Cki williams gaussian processes for machine learning mit press, Cambridge, MA.
- [36] Ibsr dataset <http://www.nitrc.org/projects/ibsr>.
- [37] J. D. Lafferty, A. McCallum, F. C. N. Pereira, Conditional random fields: Probabilistic models for segmenting and labeling sequence data, in: *Proceedings of the Eighteenth International Conference on Machine Learning*, Morgan Kaufmann Publishers Inc., San Francisco, CA, USA, 2001, pp. 282–289.
- [38] X. He, R. S. Zemel, M. A. Carreira-Perpiñán, Multiscale conditional random fields for image labeling, in: *Proceedings of the 2004 IEEE Computer Society Conference on Computer Vision and Pattern Recognition*, IEEE Computer Society, Washington, DC, USA, 2004, pp. 695–703.
- [39] P. Krähenbühl, V. Koltun, Efficient inference in fully connected CRFs with gaussian edge potentials, in: *Proceedings of the 24th International Conference on Neural Information Processing Systems*, Curran Associates Inc., USA, 2011, pp. 109–117.
- [40] S. Zheng, S. Jayasumana, B. Romera-Paredes, V. Vineet, Z. Su, D. Du, C. Huang, P. H. S. Torr, Conditional random fields as recurrent neural networks, in: *Proceedings of the 2015 IEEE International*

- Conference on Computer Vision (ICCV), IEEE Computer Society, Washington, DC, USA, 2015, pp. 1529–1537.
- [41] C. Bhole, C. Pal, D. Rim, A. Wismüller, 3D segmentation of abdominal CT imagery with graphical models, conditional random fields and learning, *Machine Vision and Applications* 25 (2) (2014) 301–325. doi:10.1007/s00138-013-0497-x.
 - [42] M. G. Uzunbas, C. Chen, D. Metaxas, An efficient conditional random field approach for automatic and interactive neuron segmentation, *Medical Image Analysis* 27 (2016) 31–44. doi:10.1016/j.media.2015.06.003.
 - [43] K. Kamnitsas, C. Ledig, V. F. Newcombe, J. P. Simpson, A. D. Kane, D. K. Menon, D. Rueckert, B. Glocker, Efficient multi-scale 3D CNN with fully connected CRF for accurate brain lesion segmentation, *Medical Image Analysis* 36 (2017) 61–78. doi:10.1016/j.media.2016.10.004.
 - [44] S. M. Smith, Fast robust automated brain extraction, *Human Brain Mapping* 17 (3) (2002) 143–155. doi:10.1002/hbm.10062.
 - [45] D. W. Shattuck, S. R. Sandor-Leahy, K. A. Schaper, D. A. Rottenberg, R. M. Leahy, Magnetic resonance image tissue classification using a partial volume model, *NeuroImage* 13 (5) (2001) 856–876. doi:10.1006/nimg.2000.0730.
 - [46] R. W. Cox, AFNI: software for analysis and visualization of functional magnetic resonance neuroimages, *Computers and Biomedical Research* 29 (3) (1996) 162–173. doi:10.1006/cbmr.1996.0014.
 - [47] S. G. Mueller, M. W. Weiner, L. J. Thal, R. C. Petersen, C. Jack, W. Jagust, J. Q. Trojanowski, A. W. Toga, L. Beckett, The alzheimer’s disease neuroimaging initiative, *Neuroimaging Clinics* 15 (4) (2005) 869–877. doi:10.1016/j.nic.2005.09.008.
 - [48] Lpba dataset <http://sve.loni.ucla.edu/>.
 - [49] Oasis dataset <http://www.oasis-brains.org/>.